1-28-2015

COMPARISON ON DIFFERENT DISCRETE FRACTIONAL FOURIER TRANSFORM (DFRFT) APPROACHES

Ishwor Bhatta

Candidate

Department

This thesis is approved, and it is acceptable in quality and form for publication:

Approved by the Thesis Committee:

, Chairperson

by

THESIS

Submitted in Partial Fulfillment of the
Requirements for the Degree of

The University of New Mexico
Albuquerque, New Mexico

Dedication

I dedicate this work to my parents for their support and encouragement.

'I am a slow walker, but I never walk back'

– Abraham Lincoln

Acknowledgments

First of all, I heartily appreciate Dr. Balu Santhanam, my advisor and thesis chair, for continuing to encourage me through the years of classroom teachings and the long number of months writing and rewriting these chapters. I hope to emmulate his professional style as I continue my career.

I also want to thank the members of my thesis committee, Dr. Maria Cristina Pereyra and Dr. Majeed Hayat.

I want to thank Dr. Mark Gilmore, Ex-director of the ECE Graduate Program and Dr. Sudharman Jayaweera, Director of the ECE Graduate Program, for appointing me as a Project Assistant at the Electrical and Computer Engineering Department for several semesters. This position helped me to gain some experience in working with students and, most importantly, to financially support my education.

I also want to thank Dr. Ramiro Jordan who played a very important role in different aspects of this journey.

I greatly appreciate the time that I spent with Dr. Edward D. Graham, Jr., Dr. Tarief Elshafiey, and Dr. Charles B. Fleddermann. I want to thank all of them for giving me an opportunity to work with them as a Grader Assistant.

I would like to thank my friends, Anees Abrol and Eric Hamke for their support and unconditional friendship.

I would also like to thank Judy Duane for her help on correcting this manuscript.

I would like to thank my uncle, Ramesh Devkota, and my aunt, Rupa Sapkota for their suppot throughout this endeavour.

Finally, I would like to express my deepest gratitude to my parents for their support and encouragement, to my brother, who has been encouraging me to persue my desires through the years, and to my sister, who has always been there to boost me up whenever I am in difficulties.

Last but not least, I praise God, the Almighty for providing me with this opportunity and for granting me the ability to persume my goals successfully.

Comparison on Different Discrete Fractional Fourier Transform(DFRFT) Approaches

by

Ishwor Bhatta

B.E., Electronics and Communication, Purbanchal University, Nepal, 2012

M.S., Electrical Engineering, University of New Mexico, 2014

Abstract

As an extension of conventional Fourier transform and a time-frequency signal analysis tool, the fractional Fourier transforms (FRFT) are suitable for dealing with various types of non-stationary signals. Taking advantage of the properties and non-stationary features of linear chirp signals in the Fourier transform domain, several methods of extraction and parameter estimation for chirp signals are proposed, and a comparative study has been done on chirp signal estimation.

Computation of the discrete fractional Fourier transform (DFRFT) and its chirp concentration properties are dependent on the basis of DFT eigenvectors used in the computation. Several DFT-eigenvector bases have been proposed for the transform, and there is no common framework for comparing them. In this thesis, we compare several different approaches from a conceptual viewpoint and point out the differences between them.

We discuss five different approaches, namely: (1) the bilinear transformation method, (2) the Grunbaum method, (3) the Dickenson-Steiglitz method, also known as the S-matrix method, (4) the quantum mechanics in finite dimension(QMFD) method, and (5) the higher order S-matrix method, to find centered-

DFT (CDFT) commuting matrices and the various properties of these commuting matrices. We study the nature of eigenvalues and eigenvectors of these commuting matrices to determine whether they resemble those of corresponding continuous Gauss-Hermite operator. We also measure the performance of these five approaches in terms of mailobe-to-sidelobe ratio, 10-dB bandwidth, quality factor, linearity of eigenvalues, parameter estimation error, and, finally peak-to-parameter mapping regions. We compare the five approaches using these several parameters and point out the best approach for chirp signal applications.

Contents

List of Figures

List of Tables

Abbreviations

2D	2-Dimensional
BW	Bandwidth
CDFRFT	Centered Discrete Fractional Fourier Transform
CDFT	Centered Discrete Fourier Transform
c_r	Chirp Rate
D-S	Dickinson-Steiglitz
DFT	Discrete Fourier Transform
DFRFT	Discrete Fractional Fourier Transform
FFT	Fast Fourier Transform
FRFT	Fractional Fourier Transform
G-H	Gauss-Hermite
HGL	Hermite-Gauss Like
MACDFRFT	Multiple Angle-Centered Discrete Fractional Fourier Transform
MLE	Maximum Likelihood Estimators
MLSLR	Mainlobe-to-Sidelobe Ratio
QMFD	Quantum Mechanics in Finite Dimensions
QMOD	Modified QMFD(QMFD with Gauss-Hermite separation)
SNR	Signal-to-Noise Ratio
w_c	Central Frequency

Chapter 1

Introduction

1.1 Overview

Stationary signals are well analyzed using the DFT. The DFT is a widely used transform since it can be implemented in a very efficient way using the FFT algorithm. However, many actual signals are non-stationary by nature. In some of these signals, we could assume the signal might be stationary, if we choose short segments, for instance; human speech. In general, analyzing non-stationary signals using the DFT is not a good choice.

To incorporate the variability of the non-stationary signal parameters, it is necessary to consider extensions of the Fourier-based representations that provide instantaneous frequency information for multi-component signals. The FRFT is a generalization of the conventional Fourier transform. It was introduced by Namias [1] in 1980, and since then it has been applied to different problems in signal processing and many other areas.

The discrete FRFT, a discrete version of the continuous FRFT, has become a vital tool for chirp signal analysis and parameter estimation. Computation of this transform and its use in chirp parameter estimation are dependent on the basis of the eigenvectors and its eigenvalues used in this computation. Several bases of DFT-eigenvectors derived from matrices that commute with DFT have been proposed.

But there is no common framework to compare those bases of DFT-eigenvectors. In this thesis we compare these bases of DFT-eigenvector to find which basis is the best one to use in chirp signal analysis. For the puropose of comparison, we have used five different bases, namely, (1) the bilinear transform basis, (2) the Grunbaum basis, (3) the infinite order second derivative approximation basis, (4) the quantum mechanics in finite dimension(QMFD) basis and (5) the Dickenson-Stieglitz basis, which are discussed individually in the later sections of the thesis. All the above mentioned sets of eigenvector bases are approximations of the G-H functions. Therefore, the application of the DFRFT to a sampled chirp will result in a peak in the 2-D plane. However, unlike the continuous version of FRFT, there are no known closed form solutions for the mapping between peak location and chirp parameter (chirp rate and central frequency). Prior work has assumed that this mapping is a sampled version of the mapping for the continuous FRFT, but this is only accurate for very narrowband chirps and not suitable for wideband signals because the basis functions of the continuous FRFT are not band-limited. Therefore, the sampling process produces aliasing, and if we do oversampling it translates to a non-orthogonal basis [2].

Prior work has used the norm of the error between the eigenvectors and sampled G-H functions to compare them. However, error-norm estimation alone is not sufficient for a thorough comparison. Therefore, we have used multiple parameters like the mainlobe-to-sidelobe ratio, 10-dB bandwidth, quality factor, liniarity of eigenvalues, error-norm of eigenvectors, 2D peak estimation error, percentage of points where peak to parameter mapping is satisfied, etc., which are described individually in the later sections of this thesis. We compute these for the proposed five different methods, and this shows that each basis is considerably different from each other.

1.2 Fractional Fourier Transform

The fractional Fourier transform (FRFT) is a family of linear transformations which generalize the Fourier transform. It can be thought of as the Fourier trans-

form to the nth power, where n need not to be an integer. Thus, it can transform a function to any intermediate domain between time and frequency. Although the continuous FRFT has existed for many years, it is only in recent years that it has been used for signal processing. In particular, it has been shown that there is close relationship between the linear chirp signal and the continuous FRFT. For any real α, the α-angle FRFT of a function f is denoted by $\mathbf{F}_\alpha(u)$ and defined by

$$\mathbf{F}_\alpha(u) = \sqrt{\frac{1-\jmath\cot(\alpha)}{2\pi}} \exp\left(\frac{\jmath\pi\cot(\alpha)u^2)}{2}\right) \int_{-\infty}^{\infty} I_\alpha f(x)dx, \tag{1.1}$$

where $I_\alpha = \exp\left(-\jmath 2\pi\left(\csc(\alpha)ux - \frac{\cot(\alpha)}{2}x^2\right)\right)$.

For $\alpha = \frac{\pi}{2}$, this becomes precisely the definition of the continuous Fourier transform, and for $\alpha = \frac{-\pi}{2}$, it is the definition of the inverse continuous Fourier transform.

In other words, The FRFT is an integral transform

$$\mathbf{F}_\alpha(u) = \int K_\alpha(u,x)f(x)dx, \tag{1.2}$$

where $\mathbf{K}_\alpha(u,x)$ is the transformation kernel defined as

$$\mathbf{K}_\alpha(u,x) = \begin{cases} \sqrt{\frac{1-\jmath\cot(\alpha)}{2\pi}}\exp(\jmath A_\alpha), & \text{if } \alpha \text{ is not a miltiple of} \pi \\ \delta(u-x), & \text{if } \alpha \text{ is a multiple of } 2\pi \\ \delta(u+x), & \text{if } \alpha+\pi \text{ is a multiple of } 2\pi \end{cases}, \tag{1.3}$$

where $A_\alpha = \left(\frac{x^2+u^2}{2}\cot(\alpha) - ux\csc(\alpha)\right)$, and it is important to observe that the kernel is continuous everywhere in α; and in particular, at multiples of π, it is seen that

$$\lim_{\alpha\to n\pi} \mathbf{K}_\alpha = \mathbf{K}_{n\pi}, \tag{1.4}$$

Substituting this kernel in the integral of the FRFT, we obtain

$$\mathbf{F}_\alpha(u) = \begin{cases} \sqrt{\frac{1-\jmath\cot(\alpha)}{2\pi}} \exp\left(\jmath\left(\frac{u^2}{2}\cot(\alpha)\right)\right) \int_{-\infty}^{\infty} f(x)\exp\left(\jmath B_\alpha\right) dx, & \text{if } \alpha = k\pi \\ f(x), & \text{if } \alpha = 2k\pi \\ f(-x), & \text{if } \alpha + \pi = 2k\pi \end{cases}, \tag{1.5}$$

where $B_\alpha = \left(\frac{x^2}{2}\cot(\alpha) + ux\csc(\alpha)\right)$ and k = integer.

1.3 Discrete Fractional Fourier Transform

In a similar way as the FRFT is based on the continuous Fourier transform, the definition of a DFRFT is based on the DFT. Since the DFT is an operator that can be expressed as a matrix vector multiplication, the starting point to define a DFRFT is the well-known eigenvalue-eigenvector decomposition of a matrix. DFRFTs have been developed by different researchers and can be put in a general form as [3];

$$\mathbf{A}_\alpha(x) = \mathbf{W}^{\frac{2\alpha}{\pi}(x)} = \mathbf{V}\Lambda^{\frac{2\alpha}{\pi}}\mathbf{V}^{-1}x, \tag{1.6}$$

where $\mathbf{W}$ is a DFT matrix, $\mathbf{V}$ is an eigenvector of DFT eigenvectors and Λ is a diagonal matrix of DFT eigenvalues.

In the case of the DFT, the eigenvectors are not only linearly independent, but are also orthonormal, and in this case the inverse of the eigenvector can be substituted by its hermitian. For a DFT matrix $\mathbf{W}$,

$$\mathbf{W} = \mathbf{V}\Lambda\mathbf{V}^{-1}. \tag{1.7}$$

Then equation 1.6 can be rewritten as

$$\mathbf{A}_\alpha(x) = \mathbf{W}^{\frac{2\alpha}{\pi}(x)} = \mathbf{V}\Lambda^{\frac{2\alpha}{\pi}}\mathbf{V}^{H}x. \tag{1.8}$$

When $\mathbf{A}_\alpha$ is evaluated for parameter value $\alpha = 0, \frac{\pi}{2}, 2\pi$ we obtain,

$$\mathbf{A}_{2\pi} = \mathbf{I}, \quad \mathbf{A}_{\frac{\pi}{2}} = \mathbf{W}, \quad \mathbf{A}_{\pi} = \mathbf{W}^2.$$

1.4 Discrete Rotational Fourier Transform

A first discussion on DFRFT was introduced by Santhanam and McClellan in [3]. This transform was called *rotational* to emphasize the fact that it implies a rotation in the time-frequency plane.

The formulation of DFRFT as a linear combination of integer power of the DFT matrix is simple and elegant, but the resulting transform does not resemble the behavior of the continuous version. The expression given in [3] is based on a grouping of eigenvalues that results in eigenvectors of the DFT that are linearly independent but form a non-orthogonal basis. The DFT matrix has only four eigenvalues (1, -1, j, -j) regardless of its size for N $\geq$ 4 [4]. Therefore we have repeated eigenvalues for N $>$ 4. The fact that the DFT has repeated eigenvalues for N $>$ 4 produces two problems when a fractional DFT is defined as expressed in equation (1.8). The first problem is that the DFT has several sets of orthogonal eigenvectors. For a matrix to have a complete set of orthogonal eigenvectors, it has to have unique eigenvalues [5]. Since this is not the case for DFT, there are multiple sets of orthogonal eigenvectors.

N	1	-j	-1	j
4m	m+1	m	m	m-1
4m+1	m+1	m	m	m
4m+2	m+1	m	m+1	m
4m+3	m+1	m+1	m+1	m

Table 1.1: Multiplicities of DFT eigenvalues

The second problem is the ambiguity in deciding the eigenvectors of the DFT kernel matrix. Because any linear combinations of the DFT eigenvectors with the same eigenvalue are still DFT eigenvectors, there is ambiguity in deciding the eigenvectors of the DFT. The multiplicities of the eigenvalues of the DFT are shown in Table 1.1. From this table, we can observe that the DFT has non-uniform eigenvalues distribution when N is a multiple of four.

1.5 Organization of Thesis

In this thesis, we compare the different algorithms used for the computation of DFRFT using different comparison parameters. We studied the different properties of five different centered DFT commuting matrices and found the best algorithm for chirp signal applications. In chapters 2 through 5, this thesis is organized as follows;

The definition of a CDFRFT is discussed in Chapter-2. The eigenvectors, the basis functions, and some of its properties are explained. In this chapter we also studied the relationship between the defined transform and discrete linear chirp signals. The ability to concentrate chirp signal into a few transform coefficients was studied. A relation between the chirp rate and the angle of the transform is also presented in this chapter.

In Chapter-3, we discuss the five different centered DFT commuting matrices. We studied the nature of eigenvalues and eigenvectors of those commuting matrices to see whether those eigenvalues and eigenvectors resemble that of corresponding continuous G-H operator. We also plotted the error-norm of the eigenvectors to analyze how far the eigenvectors are from that of continuous G-H operator. Lastly, we looked at the valid mapping region for peak-to-parameter mapping to check the connectivity and adjacency criteria of the commuting matrices.

Chapter-4 is dedicated to the purposes of comparison. We compare the performance of five different CDFT commuting matrices based on 7 various parameters.

Finally, in Chapter-5, we conclude our research and discuss topics for future research.

Chapter 2

Discrete Fractional Fourier Transform

This chapter is mainly focused on the detailed analysis of the CDFRFT. We discussed the centered DFT and its eigenvalues and eigenvector, and then we studied the DFRFT. The rest of the chapter is dedicated to the Centered DFT (CDFT) commuting matrix and to the linear chirp signals.

2.1 Discrete Fractional Fourier Transform

As an approach to solving the two problems discussed in the previous chapter, Pei and Yeh [6] proposed an improved transform which addresses the issue of ambiguity in deciding the fractional power of eigenvalues and ambiguity in deciding the eigenvectors of the DFT kernel matrix, by narrowing the choice to a single set of eigenvectors obtained from a Dickenson-Stieglitz DFT commuting matrix. The matrix $\mathbf{S}$ defined by Dickenson and Stieglitz is given as,

$$\mathbf{S} = \begin{pmatrix} 2 & 1 & 0 & \dots & 0 & 1 \\ 1 & 2\cos\omega & 1 & \dots & 0 & 1 \\ \vdots & \vdots & \vdots & \ddots & \vdots & \vdots \\ 0 & 0 & 0 & \dots & 2\cos(N-2)\omega & 1 \\ 1 & 0 & 0 & \dots & 1 & 2\cos(N-1)\omega \end{pmatrix} \tag{2.1}$$

where $\omega = \frac{2\pi}{N}$.

Matrix **S** commutes with the DFT matrix, and its eigenvectors are also the eigenvectors of DFT matrix, but they correspond to different eigenvalues, except for the case when the size of the matrix a is multiple of 4. Apart from this particular case, as **S** is a symmetric matrix, the eigenvalues of matrix **S** are all real, and the eigenvectors are orthonormal to one another, so that matrix **S** can play the same role as Hermite function plays in a continuous case.

The other problem that is addressed in Pei's method is ambiguity in deciding the eigenvectors of the DFT kernel matrix. This problem is solved by creating a separate rule of assignment that gives a different eigenvalue to each eigenvector. This rule is inspired by the fact that the eigenvalues of the FRFT are $e^{-\jmath n\alpha}$ and the eigenvectors are Hermite functions. The nth order Hermite function has n zeros; thus one can use the number of sign changes in the eigenvectors of matrix **S** to determine the Hermite order to which the eigenvectors of DFT matrix correspond. If the eigenvector has k sign changes, it plays the same role as the kth order Hermite function in the continuous case. Table 2.1 shows the eigenvalue-assignment rule for various cases of N.

N	Eigenvalues
4m	$\mathrm{e}^{-\jmath k\alpha}, k = 0, 1, 2, ..., (4m-2), 4m$
4m+1	$\mathrm{e}^{-\jmath k\alpha}, k = 0, 1, 2, ..., (4m-1), 4m$
4m+2	$\mathrm{e}^{-\jmath k\alpha}, k = 0, 1, 2, ..., 4m, (4m+2),$
4m+3	$\mathrm{e}^{-\jmath k\alpha}, k = 0, 1, 2, ..., (4m+1), (4m+2)$

Table 2.1: Eigenvalue-assignment rule of DFRFT kernel matrix

The rule defines a set of eigenvalues that have equal angular spacing on the unit circle due to parameter k, and the spacing is modified with the fractional power of parameter α. It is important to note that with this definition of fractional powers,

as α goes from 0 to $\frac{\pi}{2}$, the eigenvalues move around the unit circle, and the larger the k the larger the number of times they loop around the unit circle. Pei and Yeh showed that the results of this transform display some similarity to the continuous counterpart. They also showed that the fractional transform they define yields the DFT when $= \frac{\pi}{2}$.

2.2 Centered DFT

The DFT maps the samples of x[n], n = 1,2,.....,N to $[0, 2\pi]$ discrete frequency space with an interval 2π = N, whereas the CDFT maps to $[-\pi, \pi]$, space assuming $n = -\frac{N-1}{2}$ to $\frac{N-1}{2}$. Santhanam and Vargas-Rubio [15] discussed the CDFT operator A as the N * N matrix with entries

$$\mathbf{A}_{m,n} = \frac{1}{\sqrt{N}} e^{\left(-\jmath \frac{2\pi}{n}(m-\frac{N-1}{2})(n-\frac{N-1}{2})\right)}, \tag{2.2}$$

where m,n = 0,1,2,.....,N-1.

They have stated that the matrix defined in (2.2) is strictly centered, and the argument of the exponential has a negative sign when it is used in signal processing. Their definition of DFT results in a matrix that is the inverse of the centered matrix used by Mugler and Clary [8], and since a matrix commutes with its inverse, their CDFT has the same commuting matrix. The factor $\frac{1}{\sqrt{N}}$ is used in the definition because it is required to have a unitary transform, although in the original definition of the DFT it is not used. With $\mathbf{W}_N = e^{-\jmath \frac{2\pi}{N}}$, we can rewrite equation (2.1) as

$$\mathbf{A}_{m,n} = \frac{1}{\sqrt{N}} \mathbf{W}_N^{mn} \mathbf{W}_N^{-n\frac{N-1}{2}} \mathbf{W}_N^{-m\frac{N-1}{2}} \mathbf{W}_N^{(\frac{N-1}{2})^2}. \tag{2.3}$$

In expression (2.3), the first term is conventional DFT and the last term is a constant. The remaining two factors are also powers of $\mathbf{W}_N$ whose properties depend on the choice of N. When N is odd, the effect is equivalent to a shift in rows and columns, because the powers of $\mathbf{W}_N$ for those factors are integer.

In the case of even N, the powers are fractional, and the effect is not a simple shift in rows and columns. This means that when computing the CDFT there is no coefficient for zero frequency, and in some cases this may be an issue. This problem can be solved by shifting the signal to be transformed by a frequency of $\pm\frac{\pi}{N}$. This can be achieved by multiplying the signal with a complex signal $e^{\pm \jmath\pi\frac{n}{N}}$. If we need the DC component of a signal, this *frequency shift* procedure will produce a DC component coefficient from the CDFT when N is even [15].

2.2.1 Eigenvalue of CDFT

One of the reasons to choose the CDFT as the starting point for defining the fractional transform is that there is a fundamental difference in the multiplicities of the eigenvectors with respect to the regular DFT that can be exploited to simplify the computations. As defined by Mehta [9], the eigenvalues for the DFT matrix of size N follow the sequence

$$1, (-j)^2, (-j)^3, ..., (-j)^N, \tag{2.4}$$

while the eigenvalues for the CDFT have the sequence

$$1, (-j), (-j)^2, (-j)^3, ..., (-j)^{N-1}. \tag{2.5}$$

Comparing these two sequences, we can see that the value (-j) is skipped in the eigenvalues of DFT. The result of this difference is that when N is a multiple of 4, the DFT has different multiplicities for the 4 eigenvalues, while, in this case, the CDFT has the multiplicity of N/4 for each eigenvalue as is shown in Table 2.2. The consequence of the different multiplicities of the eigenvalues of the DFT is that the diagonal matrix of fractional power $\Lambda^{\frac{2\alpha}{\pi}}$ requires two different definitions for the cases of N, even and odd. When we use the CDFT to define a fractional power we can use a single definition for all values of N give as,

$$\Lambda^{\frac{2\alpha}{\pi}} = diag(e^{-\jmath p\alpha}),\ with\ 0\ \leq p \leq N-1. \tag{2.6}$$

N	CDFT			
	1	-j	-1	j
4m	m	m	m	m
4m+1	m+1	m	m	m
4m+2	m+1	m+1	m	m
4m+3	m+1	m+1	m+1	m

Table 2.2: Multiplicities of the eigenvalues of the CDFT

2.2.2 CDFT Commuting Matrices and Their Eigenvectors

Having only four different eigenvalues, we know that for N > 4 the CDFT matrix does not have a unique set of orthogonal eigenvectors, and we have the same problem as with the DFT. In order to define a fractional transform we need an orthogonal set of eigenvectors for the CDFT matrix. As we have described in the previous chapter, the solution that has been used by many of the researchers is to use the eigenvectors of the CDFT commuting matrices. From matrix theory [5], we know that a pair of matrix **A** and **B** that commute, i.e. **AB** = **BA**, have a common set of eigenvectors.

We are using five different bases, which are described later in the thesis, to obtain the CDFT commuting matrix. All the eigenvalues obtained from those 5 bases have multiplicity one, therefore, its eigenvectors are orthogonal. We use the eigenvector of those 5 matrices to construct the fractional transform. They have been presented in [10], [11], [12], [13] and [14] as discrete versions of G-H functions. The eigenvectors of those matrices look like a G-H function, however, they are not exactly the same. Figure 2.1 shows a 9th order eigenvector of G-H operator for sample size of 256. Figure 2.2 shows a 10th order eigenvector for Grunbaum method. This looks like a 9th order eigenvector of G-H operator shown in figure 2.1. The samples of the G-H function presented in figure 2.1 are taken at $x = \sqrt{\frac{2\pi}{N}}(n - \frac{N-1}{2})$ with n = 0,1,.....,N-1 for N = 256, and normalized as is done with the eigenvector. The eigenvectors are numbered by the corresponding eigenvalue of the DFT commuting matrix in ascending order. Eigenvector 1 is associated with the smallest eigenvalue.

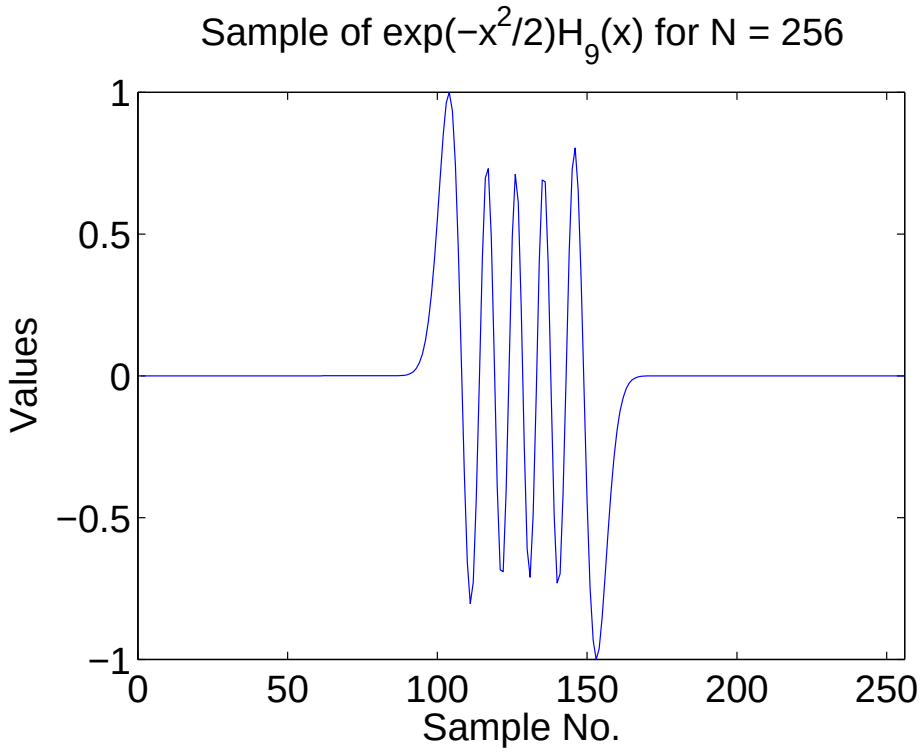

Figure 2.1: Plot of sample of G-H function

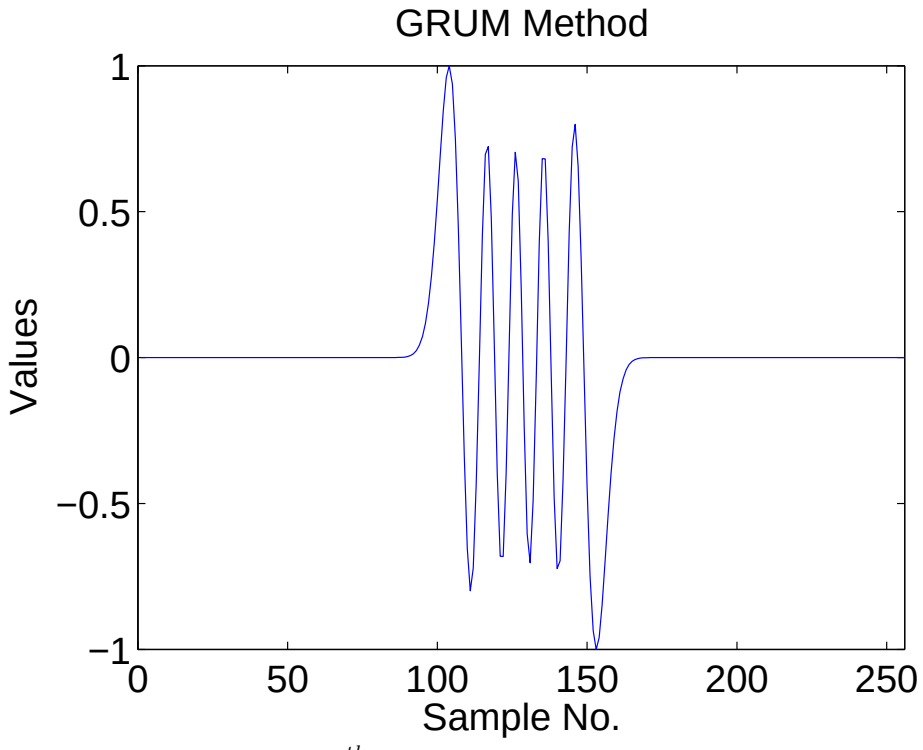

Figure 2.2: Plot of 10^{th} eigenvector of Grunbaum matrix for N = 256

2.3 Centered Discrete FRFT

Vargas-Rubio and Santhanam [15] defined the centered DFRFT (CDFRFT) for the fractional parameter α as

$$\mathbf{A}_\alpha = \mathbf{V}_T \Lambda^{\frac{2\alpha}{\pi}} \mathbf{V}_T^H, \tag{2.7}$$

where $\mathbf{V}_T$ is a matrix whose columns correspond to the orthogonal eigenvectors obtained from the commuting matrix $\mathbf{T}$. The eigenvectors are sorted in ascending order of its corresponding eigenvalue in $\mathbf{T}$ as it was explained earlier, and the first column of $\mathbf{V}_T$ corresponds to the eigenvector with smallest eigenvalue. $\Lambda^{\frac{2\alpha}{\pi}}$ is a diagonal matrix whose elements are $\lambda_k = e^{-jk\alpha}$, $0 \leq k \leq N-1$. With this substitution equation (2.7) becomes

$$\mathbf{A}_\alpha = \sum_{k=0}^{N-1} e^{-j\alpha k} \mathbf{v}_k \mathbf{v}_k^H, \tag{2.8}$$

where v_k is the eigenvector with k sign changes.

With this definition, the CDFRFT at $\alpha = \frac{\pi}{2}$ corresponds to the CDFT that is interpreted as a rotation of 90° in the time-frequency domain. If we further increase α to π, we have a time reversal transformation, and obviously with $\alpha = \frac{3\pi}{2}$, we have the inverse CDFT.

The definition assigns the eigenvectors in the standard order by the eigenvalues of $\mathbf{T}$, and it is equivalent to the assignment of the eigenvector with k sign changes to the $\lambda_k = e^{-jk\alpha}$ as is defined in [16]. In addition, this is the same correspondence we have in the continuous transform with respect to the G-H functions. There are other possible eigenvalue-eigenvector assignments that have been studied by Cariolaro and Ehrsege [17] and [18]. We will only use the assignment explained in [16] for the purpose of this thesis.

2.4 Multi-angle CDFRFT

Vargas-Rubio and Santhanam [15] discussed the multi-angle CDFRFT as;

$$\{\mathbf{A}_\alpha\}_{kn} = \sum_{p=0}^{N-1} v_{kp} v_{np} e^{-\jmath p\alpha}, \tag{2.9}$$

where v_{kp} is the kth element of the pth eigenvector. Multiplying $\mathbf{A}_\alpha$ by the signal x[n], we obtain;

$$\mathbf{X}_\alpha[k] = \sum_{n=0}^{N-1} x[n] \sum_{p=0}^{N-1} v_{kp} v_{np} e^{-\jmath p\alpha}. \tag{2.10}$$

For discrete set of angles $\alpha = \alpha_r = \frac{2\pi r}{N},\ r = 0, 1, ..., N-1$

$$\mathbf{X}_k[r] = \sum_{p=0}^{N-1} z_k[p] \mathbf{W}_N^{pr}, \tag{2.11}$$

where

$$z_k[p] = v_{kp} \sum_{n=0}^{N-1} x[n] v_{np}. \tag{2.12}$$

Expressing the transform as a DFT allows us to use a regular FFT algorithm to compute the CDFRFT. The resulting transform $\mathbf{X}_k[r]$ containing the CDFRFT for these discrete angles is called multi-angle DFRFT (MA-CDFRFT).

It is important to observe that $\mathbf{X}_k[0]$ corresponds to the original signal x[n] with k = n, and $\mathbf{X}_k[\frac{N}{4}]$ corresponds to the CDFT of x[n] when N is a multiple four, since in this case, $\alpha_{\frac{N}{4}} = \frac{\pi}{2}$. Figure 2.3 shows a graphical representation of the array $\mathbf{X}_k[r]$ to illustrate how index k has different interpretations depending on the value of r. For example, when r = 0, k is interpreted as time and when $r = \frac{N}{4}$, k corresponds to frequency. This interpretation also shows that the upper half of $\mathbf{X}_k[r]$ is a reversed version of the lower half.

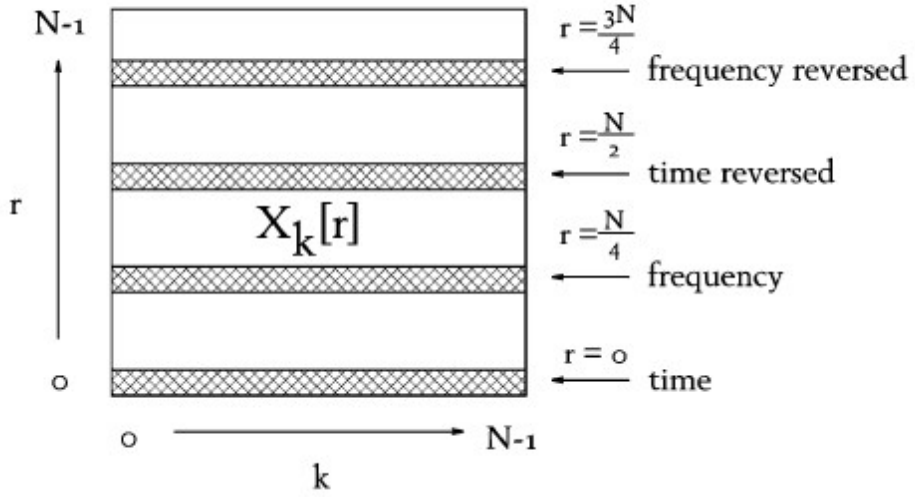

Figure 2.3: Graphical representation of $\mathbf{X}_k[r]$ that shows how the interpretation of the index k changes depending on the value of index r.

2.5 Linear Chirp Signal

One of the properties of FRFT is that its kernel includes a linear chirp signal [19]. Therefore the computation of the MA-CDFRFT can be applied to the estimation of the chirp rate of a single signal, or multicomponent signal with similar average frequency but different chirp rates [15].

2.5.1 Mono-component Chirp Signal

A complex chirp with zero average frequency can be expressed as [14],

$$x[n] = e^{\jmath c_r (n - \frac{N-1}{2})^2}, \ 0 \leq n \leq N-1, \tag{2.13}$$

where c_r is the chirp rate.

A simple experiment shows that choosing a particular angle α produces the effect of concentrating a linear chirp signal in a few coefficients of the resulting transform. For the purpose of this thesis, we used $c_r = 0.001$ and N = 256. Therefore the chirp signal becomes;

$$x[n] = e^{\jmath 0.001 (n - \frac{255}{2})^2}, \ 0 \leq n \leq 255. \tag{2.14}$$

After some trial and error with different values of α, we found that for $\alpha = 85.27$ we obtain a good concentration in a few coefficients of the transform. Figure 2.4 describes the magnitude of the MA-CDFRFT of this signal and a slice of the MA-CDFRFT matrix at the particular angle of 85.27, where the magnitude of the MA-CDFRFT is maximum. Specifically we can observe that we actually have two maxima, because the CDFRFT at $\alpha + \pi$ is the reversed version of the CDFRFT at α. The location of the maxima is at r = 69.

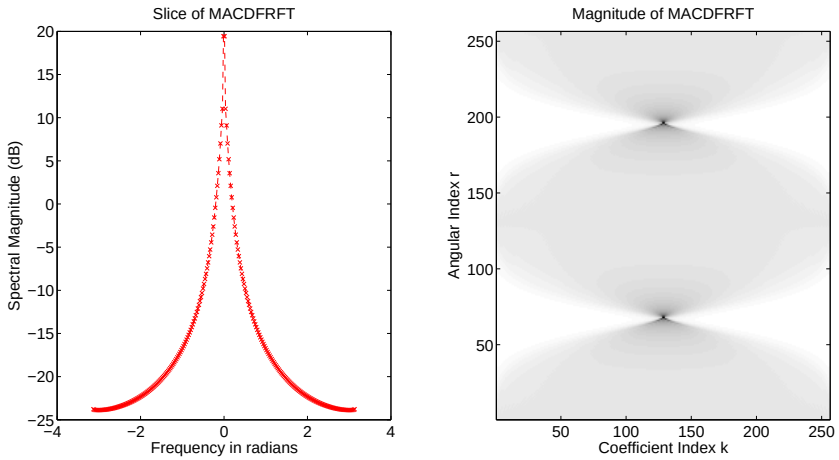

Figure 2.4: A slice of the MA-CDFRFT matrix at r = 69 and magnitude of the corresponding MA-CDFRFT for $c_r = 0.001$, $w_c = 0$, $\alpha = 85.27$, N = 256 and Grunbaum basis for monocomponent chirp with zero average frequency

2.5.2 Multi-component Chirp Signal

When the MA-CDFRFT is applied to a multicomponent signal, we were able to distinguish the different components of the signal if they had different chirp rates even when their spectra overlap.

As an example we used the signal

$$x[n] = e^{\jmath(0.005(n-\frac{127}{2})^2)} + e^{\jmath(-0.007(n-\frac{127}{2})^2)},\ n = 0, 1, 2.....,127. \tag{2.15}$$

This is a signal consisting of two linear chirps, one with a positive chirp rate, and the other with a negative chirp rate. Both signals have an average frequency equal to zero. As is shown in the image of figure 2.5, the magnitude of the transform displays four peaks, two for each signal, and it can be clearly determined that

the signal consists of two linear chirp components. We also noted that, unlike in the case of a mono-component chirp, when we had two components, we saw some fringes that result from the fact that the amplitude is no longer constant. A slice of the MA-CDFRFT matrix at r = 36 can be seen in figure 2.5.

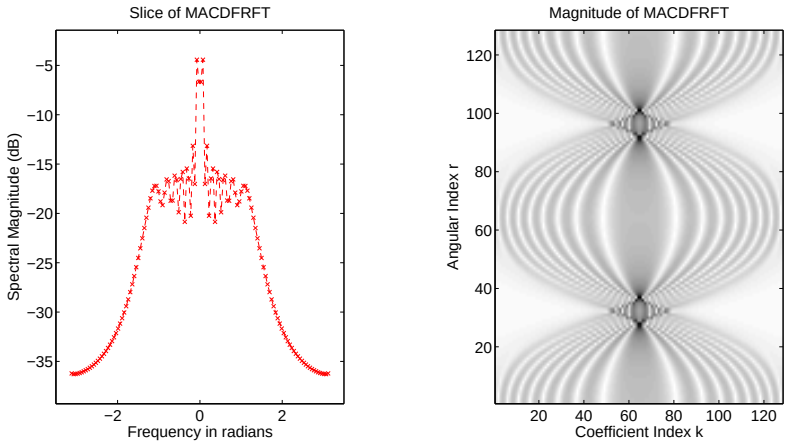

Figure 2.5: Slice of the MA-CDFRFT at r = 36 and magnitude of the corresponding MA-CDFRFT for $c_{r1} = 0.005$, $c_{r2} = -0.007$, $w_c = 0$, N = 128 and Grunbaum basis for multi-component chirp with zero average frequency

2.5.3 Chirps with non-zero average frequency

When a signal has an average frequency different from zero, the chirp signal is described as [14],

$$x[n] = e^{\jmath(c_r(n-\frac{N-1}{2})^2 + w_0(n-\frac{N-1}{2}))},\ 0 \leq n \leq N-1. \tag{2.16}$$

where w_0 is the average frequency.

For this signal, we are interested in determining where peak occurs. This is important because we are interested in knowing how well the CDFRFT can localize the average frequency of the signal.

We chose $w_0 = \frac{\pi}{4}$ with $c_r = 0.001$ and N=256 to see where the peak occurred. Figure 2.6 describes the magnitude of the MA-CDFRFT of this signal and a slice of the MA-CDFRFT matrix at r = 68. As shown in the figure, the peak occurs at r = 68 and k = 160. From this figure, we can observe that the peak deviates from

the origin. Because of non-zero average frequency, it is obvious that this must occur.

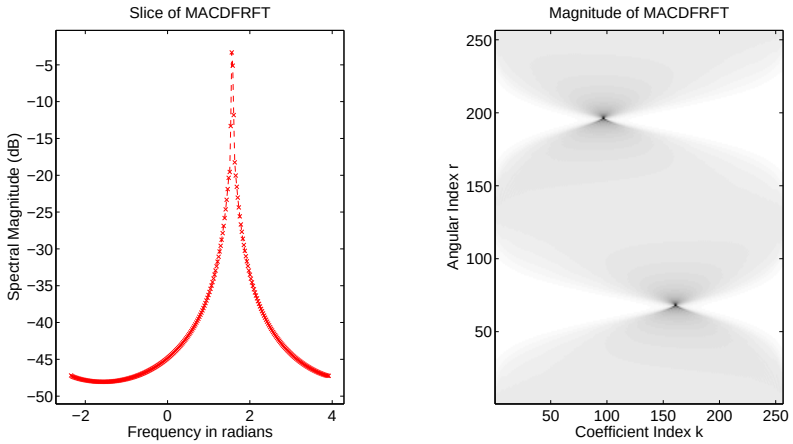

Figure 2.6: Slice of the MA-CDFRFT at r = 68 and magnitude of the corresponding MA-CDFRFTT for $c_r = 0.001$, $w_c = \frac{\pi}{4}$, N = 256 and Grunbaum basis for monocomponent chirp with non-zero average frequency

2.6 Relation between α and c_r

For better concentration of signal energy when analyzing linear chirps, an α between 45° to 135° is a good choice [15]. For this interval, an empirically developed relationship between the angle of transform and chirp rate, with corresponding error less than 2%, is given as;

$$c_r = 2\frac{\tan\left(\alpha - \frac{\pi}{2}\right)}{N} + 1.41\frac{\left(\alpha - \frac{\pi}{2}\right)}{N}, \tag{2.17}$$

with $\alpha = \frac{2\pi r}{N}$.

This relationship is useful in determining the chirp rate from the angle, particularly when we use the MA-CDFRFT algorithm.

We found the chirp rate using (2.17) for the signal we used in section 2.5.1, where we found that the peak occurs at r = 69 for N = 256,

$$\alpha = \frac{2\pi r}{N} = 1.6935,$$

and $c_r = 0.00163$. This is close to 0.001, which is the value we took in this particular case.

The MA-CDFRFT and the appropriate relations were applied to estimate the two chirp rates associated with the two-component chirp signal used in the section 2.5.2. Using equation (2.18),

$$\alpha = 1.3253 \text{ for } r\text{=27 and N=128},$$
$$\alpha = 1.7671 \text{ for } r\text{=36 and N=128},$$

and using equation (2.17) we found that

$$c_r = -0.0066 \text{ for } r\text{=27 and N=128},$$
$$c_r = 0.0052 \text{ for } r\text{=36 and N=128}.$$

Now we can observe that these chirp rates are close to -0.007 and 0.005, which we had assumed in the section 2.5.2. Table 2.3 shows the chirp rate obtained using equation (2.17). From this table we can see that the chirp rate obtained from the equation is very close to the actual chirp rate. This proves that the relationship in equation (2.17) is sufficient for chirp parameter estimation.

Actual Chirp Rate	Chirp Rate using Equation 2.17
-0.012176346	-0.011628762
-0.008356316	-0.008056398
-0.004536286	-0.004338268
-0.000716256	-0.000326968
0.003103774	0.003649013
0.006923804	0.007656638
0.010743834	0.010743834

Table 2.3: Comparison between actual chirp rate and the chirp rate obtained from equation (2.17)

Peacock and Santhanam [2] have derived an expression for peak-to-parameter mapping. Using this expression for the QMOD method, they produce a mapping region which is very similar to the continuous mapping for $\omega < \frac{\pi}{3}$,

$$\alpha = -\frac{\pi}{N}\cot\left(\frac{k\pi}{N}\right) \qquad \textit{and} \qquad \omega = \frac{2\pi}{N}\left(r - \frac{N-1}{2}\right)\csc\left(\frac{k\pi}{N}\right), \tag{2.18}$$

Actual Parameters		Parameters obtained from equation 2.24	
ω_c	C_r	$\hat{\omega_c}$	$\hat{C}_r$
$\frac{\pi}{4}$	0.001	0.8015	0.0012
$\frac{\pi}{4}$	0.002	0.7846	0.0021
$\frac{\pi}{4}$	0.003	0.7970	0.003
$\frac{\pi}{4}$	0.004	0.7883	0.004
$\frac{\pi}{4}$	0.005	0.7836	0.005
$\frac{\pi}{4}$	0.006	0.7831	0.0061

Table 2.4: Comparison of actual chirp rates and chirp rate estimates from equation 2.19

where α is chirp rateand ω is central frequency

But we found that this mapping does not correcly map the peak location to the corresponding chirp rate and central frequency.

We then modified this peak to parameter mapping expression to correctly map the peak location to the corresponding chirp rate and central frequency as

$$\hat{C}_r = -\frac{\pi}{N}\cot\left(\frac{2r_p\pi}{N}\right) \qquad and \qquad \hat{\omega_c} = \frac{2\pi}{N}\left(k_p - \frac{N-1}{2}\right)\csc\left(\frac{2r_p\pi}{N}\right), \quad (2.19)$$

where $\hat{C}_r$ is the estimatated chirp rate, $\hat{\omega_c}$ is the estimated central frequency, r_p is the coefficient index of peak location and k_p is the angular index of peak location.

With this expression, we can obtain the peak-to-parameter mapping with average error of 0.4% for the QMOD method. Therefore we can conclude that equation 2.19 produces less error in terms of parameter estimation and peak to parameter mapping in comparison to equation 2.17.Table 2.4 depicts the example of the peak to pameter mapping for the QMOD method with G-H separation using equation 2.19.

2.7 Conclusion

In this chapter, we have discussed the centered DFRFT for various eigenvector bases. We studied the eigenvalues and eigenvectors of the different commuting matrix approaches. We further compared two analytical expressions for the peak

to parameter mapping.

Chapter 3

CDFT Commuting Matrices

The FRFT has found many applications in various areas including signal processing [20], time-frequency analysis [21], quantum mechanics [1], and signal recovery [22]. FRFT is a potentially powerful tool in the analysis of chirp-type signals. As chirp signals are widely used in radar, sonar and communication systems, estimation of their parameters such as, amplitude, chirp rate, initial frequency and initial phase has been an important problem [23].

In recent years, much efforts has been invested in obtaining the DFRFT that inherits the properties of the continuous FRFT [24]. Early works on DFRFT have shown that the eigenvectors of the CDFT commuting matrices are discrete HGL functions [25]. Therefore, this chapter is dedicated to discussing the various methods that can be used to obtain CDFT commuting matrices.

3.1 The Dickinson and Steiglitz (D-S) Method

Dickinson and Steiglitz defined a DFT commuting matrix [11], whose eigenvectors look like G-H function, as

$$\mathbf{S} = \begin{pmatrix} 2 & 1 & 0 & \dots & 0 & 1 \\ 1 & 2\cos\omega & 1 & \dots & 0 & 0 \\ \vdots & \vdots & \vdots & \ddots & \vdots & \vdots \\ 0 & 0 & 0 & \dots & 2\cos(N-2)\omega & 1 \\ 1 & 0 & 0 & \dots & 1 & 2\cos(N-1)\omega \end{pmatrix}, \tag{3.1}$$

where $\omega = \frac{2\pi}{N}$.

Here the diagonal elements are $2\cos(\frac{2\pi}{N}n),\ 0 \leq n \leq N-1$. This makes the matrix $\mathbf{S}$ commute with the DFT. We have been discussing the centered DFT (CDFT) for the purpose of this thesis. If we change the range of n from $0 \leq n \leq N-1$ to $-\frac{N-1}{2} \leq\ n \leq \frac{N-1}{2}$, we will have a new $\mathbf{S}$-matrix which will commute with CDFT.

$$i.e.\ [\mathbf{W}, \mathbf{S}_{cen}] = \mathbf{W} * \mathbf{S}_{cen} - \mathbf{S}_{cen} * \mathbf{W} = 0, \tag{3.2}$$

where $\mathbf{W}$ = Centered DFT and $\mathbf{S}_{cen}$ = Centered version of S-matrix.

The 10th eigenvector of the centered $\mathbf{S}$-matrix is shown in figure 3.1(a), which looks like a 9^{th} order G-H function. The plot of eigenvalues of the G-H operator depicts a linear spacing [20]. Figure 3.1(b) shows the plot of the eigenvalues of the $\mathbf{S}$-matrix, which is not exactly a linear curve but we can say that it is nearly linear.

We also plotted the error-norm of the eigenvectors to see how close the eigenvectors were to the G-H function. For this, we first computed the Hemite-Gauss-Like (HGL) eigenvectors of a size 64×64 of the S-matrix. Then we defined the error-norm as the second norm of the difference vector between the HGL eigenvector and the corresponding G-H function. Figure 3.2 shows the error-norm for the $\mathbf{S}$-matrix method for N = 64. From the figure, it is clear that the error-norm increases as

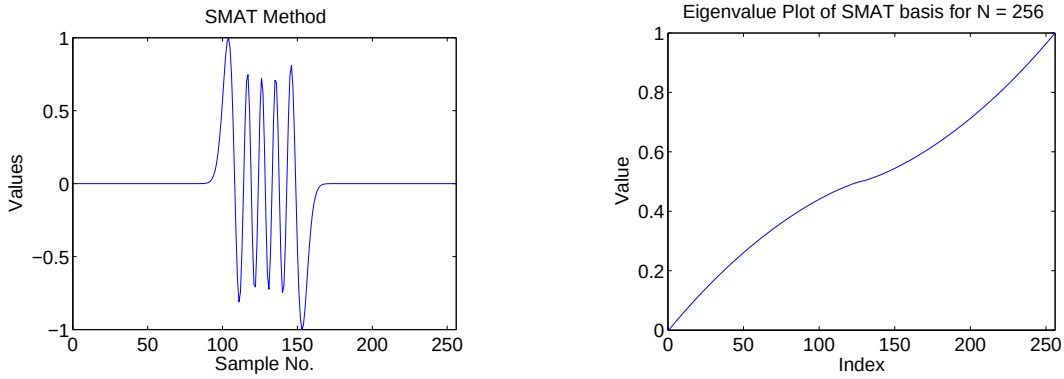

(a) (b)

Figure 3.1: (a)10^{th} eigenvector of the S-matrix for N=256 and (b) Eigenvalues of the S-matrix method for N=256

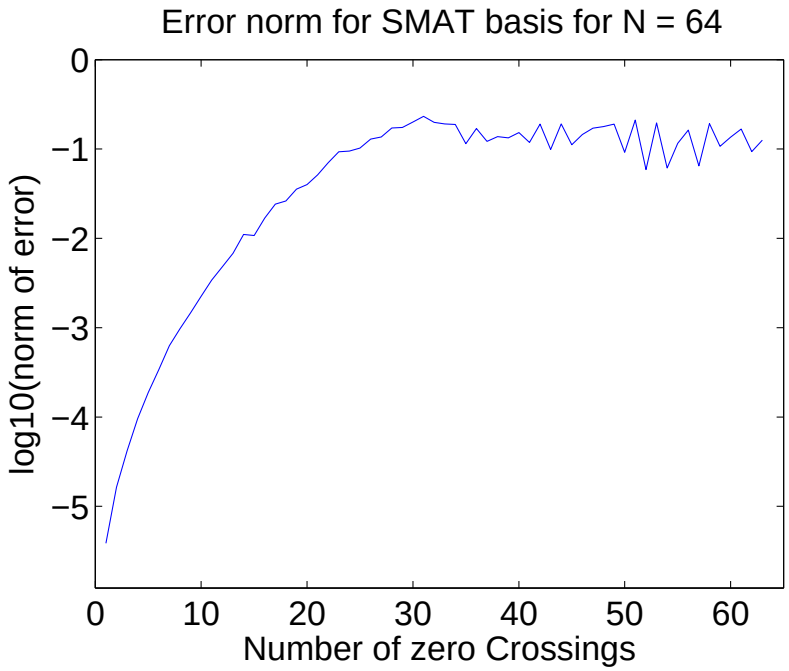

Figure 3.2: Error-norm for the S-matrix method for N = 64

the number of zero crossings increases. This is obvious because a large number of zero crossings implies a high frequency, and there is a high possibility of error for high frequency.

To further analyze the quality of the CDFT commuting matrix, we looked at the peak-to-parameter mapping. As discussed in [26], to calculate the peak-to-parameter mapping, we generated $4N \times 4N$ sample chirp functions evenly spaced in the range of $\alpha\ \varepsilon\ (0, \pi)$ and $\omega\ \varepsilon\ \left(-\frac{\pi}{N}, \frac{\pi}{N}\right)$, where α is a chirp rate and ω is the center frequency. The peaks in the DFRFT for a chirp occur roughly between $k = \frac{N}{4} \ldots \frac{3N}{4}$ and $r = \frac{N}{2} \ldots N$, where r is the location of peak in MA-CDFRFT

plane.

Application of the DFRFT to chirp parameter estimation has been discussed by many researchers. This estimation is not meaningful if a complete analysis of the invertibility of the peak-to-parameter mapping is ignored. The analysis of the invertibility of the mapping refers the following [2];

- The set of all chirp parameters that map to a single location in the chirp-rate versus center-frequency plane must form a connected set (Connectivity Criteria).
- Locations which are adjacent in the transform plane must map to adjacent regions in the chirp parameter space (Adjacency Criteria).

Figure 3.3 depicts the region in the $\alpha - \omega$ plane for the **S** -matrix method where the mappings satisfied the connectivity and adjacency conditions for chirps of length N = 256, with a transform size $N \times N$, measured using $4N \times 4N$ chirps with center frequencies and chirp rates evenly spaced over the shown area in the figure.

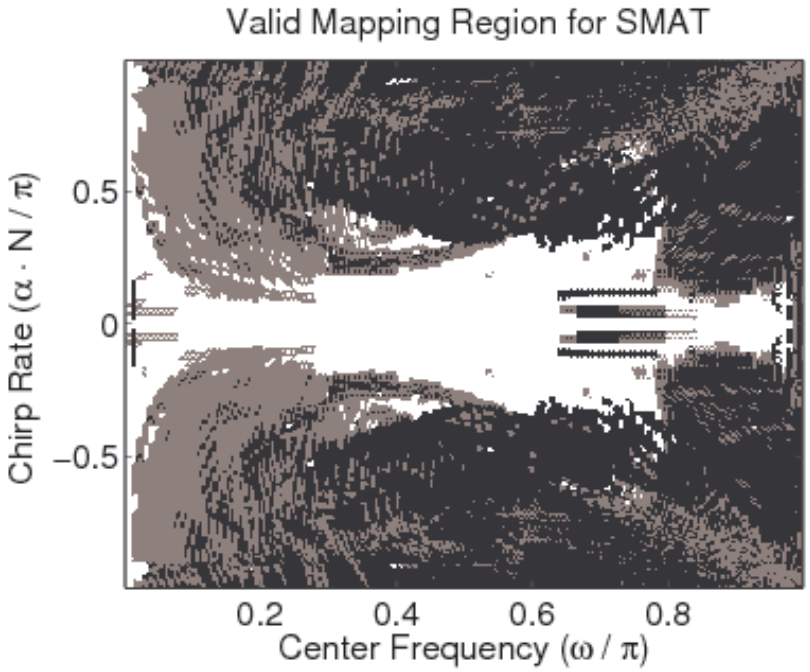

Figure 3.3: Valid mapping regions for the S-matrix method for N = 256 where black regions depict where the connectivity criteria is not satisfied, whereas the grey region depict where the adjacency criteria is not satisfied and white regions indicate that both criteria are satisfied.

This shows that the mapping region for the **S**-matrix method depicts a significantly smaller invertible region in comparison to the diamond shaped region shown in figure 3.4, where aliasing does not occur.

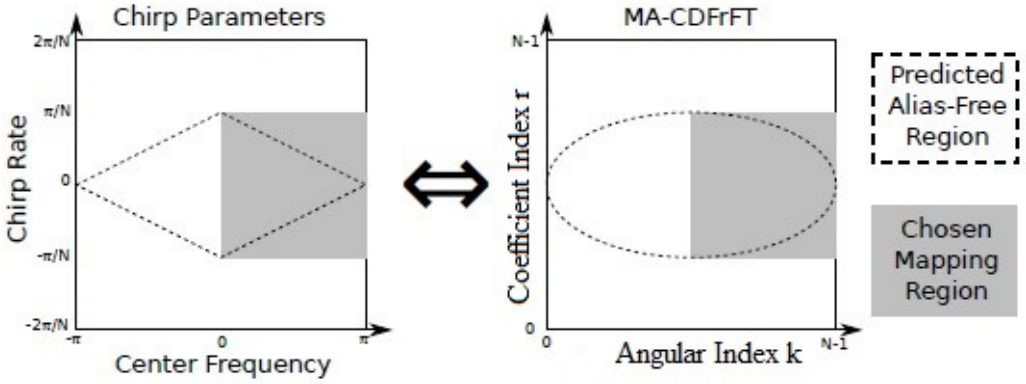

Figure 3.4: Expected valid mapping region: Outside of the dashed region, the instantaneous frequency of the chirps spills out of $w\varepsilon[-\pi,\pi]$, so the Nyquist sampling theorem is not satisfied.

3.2 The Bilinear Transformation Method

Another approach to generating a DFT commuting matrix is introduced by Serbes and Durak-Ata in [12]. They defined a new DFT commuting matrix as;

$$\mathbf{B} = \mathbf{B}_1^{-1}\mathbf{E}_2 + \mathbf{F}\mathbf{B}_1^{-1}\mathbf{E}_2\mathbf{F}^{-1}, \tag{3.3}$$

where

$$\mathbf{B}_1 = \begin{bmatrix} k & 1 & 0 & \dots & \dots & 0 & 1 \\ 1 & k & 1 & \dots & \dots & 0 & 0 \\ 0 & 1 & k & \dots & \dots & \vdots & \vdots \\ \vdots & \vdots & \vdots & \ddots & \ddots & \vdots & \vdots \\ 1 & 0 & 0 & \dots & \dots & 1 & k \end{bmatrix}. \tag{3.4}$$

$$\mathbf{E}_2 = \begin{bmatrix} -2 & 1 & 0 & \dots & \dots & 0 & 1 \\ 1 & -2 & 1 & \dots & \dots & 0 & 0 \\ 0 & 1 & -2 & \dots & \dots & \vdots & \vdots \\ \vdots & \vdots & \vdots & \ddots & \ddots & \vdots & \vdots \\ 1 & 0 & 0 & \dots & \dots & 1 & -2 \end{bmatrix}. \tag{3.5}$$

$\mathbf{F}$ = DFT matrix and $k = 10^9$ is used in this thesis.

This newly generated matrix $\mathbf{B}$ commutes with DFT. In order to make it commute with the centered version of DFT, we simply changed the off-centered DFT to a

centered DFT. After replacing **F** with its centered version we got another matrix **B** which commutes with centered DFT. i.e. $[\mathbf{B},\mathbf{F}] = \mathbf{B*F} - \mathbf{F*B} = 0$, where **F** is a centered DFT.

As we did in the previous section, we plotted the eigenvector and eigenvalues of the matrix **B** to see how close the eigenvectors were to the continuous G-H function and to see how linear the eigenvalues were. Figure 3.5(a) shows the 10^{th} order eigenvector of matrix **B** for N = 256, which looks like a 9^{th} order G-H function. Figure 3.5(b) shows the eigenvalues of matrix **B** of order 256. This plot of eigenvalues looks similar to the plot with the **S**-matrix method, which is nearly linear.

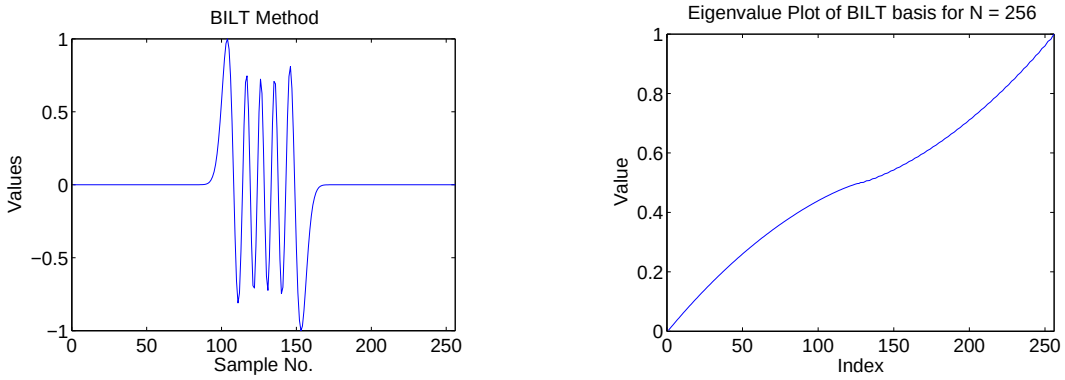

(a) (b)

Figure 3.5: (a)10^{th} eigenvector of the matrix B for N=256 and (b) Eigenvalues of the Bilinear transformation method for N=256

We plotted the error-norm of the eigenvector of matrix **B** for an order of 64 to check the error on representing the G-H function by the eigenvectors of matrix **B**. Figure 3.6 shows the error-norm for the bilinear transformation method for N = 64. This figure also shows that the error-norm decreases as the number of zero crossings increases due to the fact that we discussed in the previous section.

We plotted the valid mapping region for matrix **B** in the $\alpha - \omega$ plane to determine in which region the two conditions mentioned in the previous section were satisfied.

Figure 3.7 depicts the region in the $\alpha - \omega$ plane for the bilinear transformation method where the mappings satisfied the connectivity and adjacency conditions for chirps of length N = 256, with a transform size $N \times N$, measured using $4N \times 4N$ chirps with center frequencies and chirp rates evenly spaced over the shown

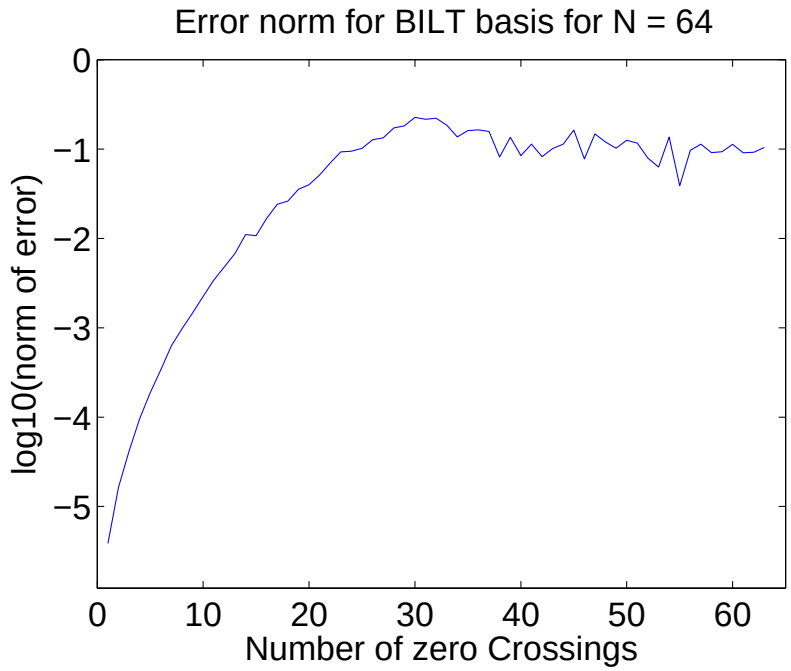

Figure 3.6: Error-norm for the bilinear transformation method for N = 64

area in the figure. From the figure, it is clear that, as in the**S**-matrix method, the mapping region for the bilinear transformation method depicts a significantly smaller invertible region in comparison to the diamond shaped region shown in figure 3.4.

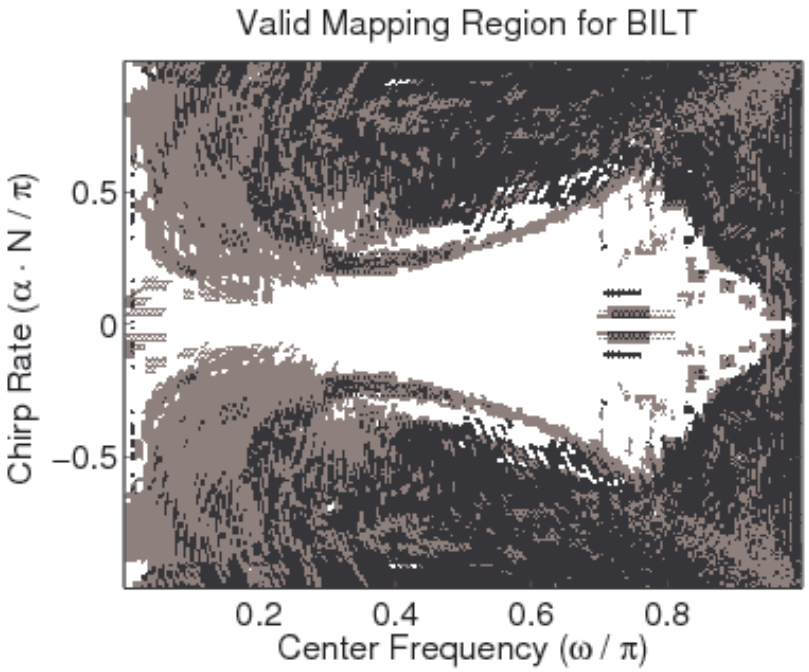

Figure 3.7: Valid mapping regions for the bilinear transformation method for N = 256

3.3 The Infinite Order Second Derivative Approximation Method

Inspired by the work of Grunbaum [27], Pei, Hsue and Ding proposed another DFT-commuting matrix in [13], whose eigenvectors are even closer to the continuous G-H function than those of the Dickinson-Steiglitz matrix. The matrix proposed by them is given as;

$$\mathbf{M}_{2k} = \sum_{m=1}^{k} (-1)^{m-1} \frac{2[(m-1)!]^2}{(2m)!} \mathbf{D}^m, \tag{3.6}$$

where

$$\mathbf{D} = \begin{bmatrix} -2 & 1 & 0 & \dots & \dots & 0 & 1 \\ 1 & -2 & 1 & \dots & \dots & 0 & 0 \\ 0 & 1 & -2 & \dots & \dots & \vdots & \vdots \\ \vdots & \vdots & \vdots & \ddots & \ddots & \vdots & \vdots \\ 1 & 0 & 0 & \dots & \dots & 1 & -2 \end{bmatrix}. \tag{3.7}$$

For the purpose of this thesis, we have used $k = 2$. Therefore, for $k = 2$;

$$\mathbf{M}_4 = \frac{-1}{12}\mathbf{D}^2 + \mathbf{D}. \tag{3.8}$$

Now the DFT commuting matrix based on this analysis is proposed as;

$$\mathbf{S}_4 = \mathbf{M}_4 + \mathbf{F}\mathbf{M}_4\mathbf{F}^{-1}. \tag{3.9}$$

We referred to this matrix $\mathbf{S}_4$, which commutes with DFT, as a higher-order S-matrix for the purpose of this thesis. If we change the off-centered DFT to its centered version, then the higher-order S-matrix will become commutable with the centered DFT. We again plotted eigenvectors and eigenvalues to compare them with those of continuous G-H operator. Figure 3.8(a) shows the 10^{th} eigenvector of higher order S-matrix for N = 256, which looks like a 9^{th} order G-H function, however it is not exactly the same. We will discuss next how much the eigenvector differs from the corresponding G-H function. Figure 3.8(b) shows the eigenvalues of higher-order S-matrix for N = 256. This shows that the eigenvalues for the

higher-order S-matrix is not as linear as that of the G-H operator; however, we can see some improvement in comparison to the Dickinson-Steiglitz method.

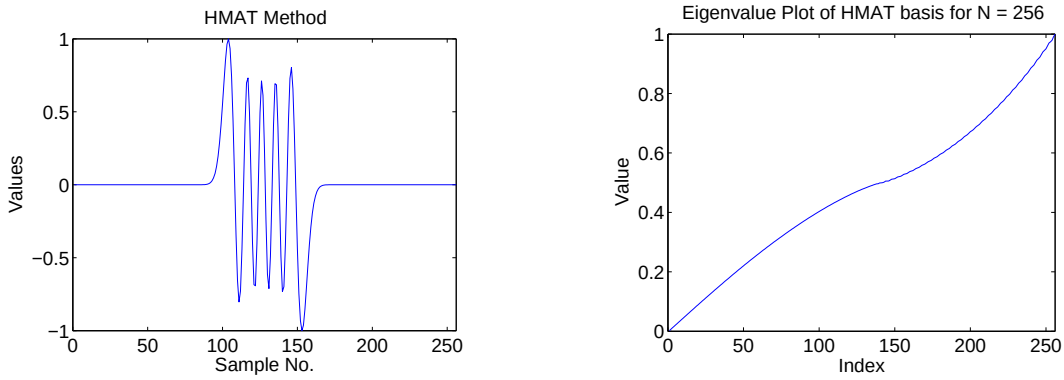

(a) (b)

Figure 3.8: (a)10^{th} eigenvector of the higher order S-matrix method for N=256 and (b) Eigenvalues of the higher order S-matrix method for N=256

Figure 3.9 shows the error-norm for the higher-order S-matrix method for N = 64. As in previous cases, the error-norm increases with the increase in number of zero crossings; however we can also see that the error-norm for the higher-order S-matrix seems less for a lower number of zero crossings in comparison to the S-matrix method.

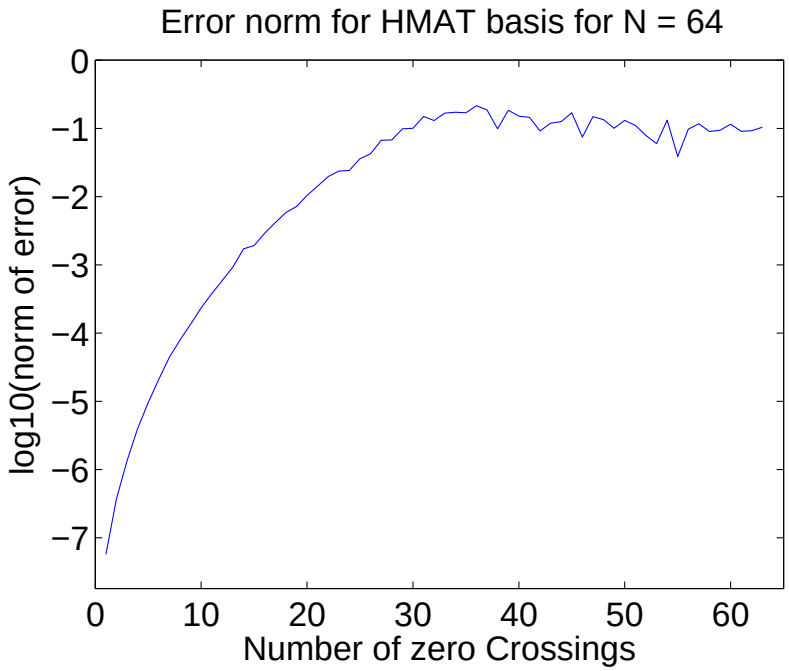

Figure 3.9: Error-norm for the higher-order S-matrix method for N = 64

Figure 3.10 shows the region in the $\alpha - \omega$ plane for the higher-order S-matrix method where the mappings satisfied the connectivity and adjacency conditions

for chirps of length N = 256, with a transform size $N \times N$, measured using $4N \times 4N$ chirps with center frequencies and chirp rates evenly spaced over the shown area in the figure. As in previous cases, the higher-order S-matrix method also has a smaller invertible region for peak-to-parameter mapping [26].

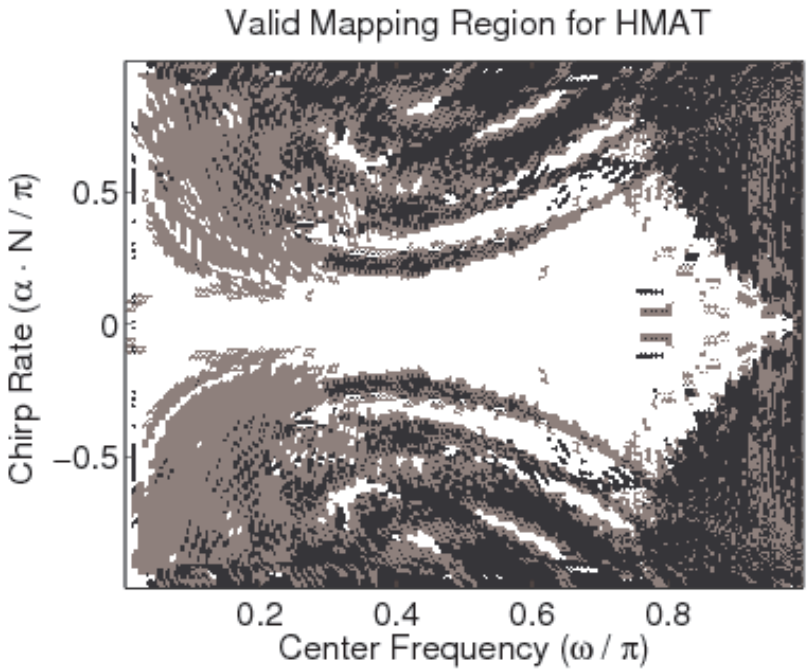

Figure 3.10: Valid mapping regions for the higher order S-matrix method for N = 256

3.4 The Grunbaum Method

Another approach to obtaining the DFT eigenvectors uses the tri-diagonal commuting matrix introduced by Grunbaum [27]. Mugler and Clary modified the Grunbaum tri-diagonal incorporating a scaling factor, and the resultant eigenvectors very closely resemble the G-H operators [28]. The tri-diagonal commuter of Grunbaum is defined via its diagonal and off-diagonal elements in [28] as;

$$\mathbf{T}_{mn} = \begin{cases} -2\cos(\pi N\tau)\sin(\pi\mu\tau)\sin(\pi(N-\mu-1)\tau), & \text{if m = n ,0} \leq \text{ n } \leq \text{ N-1} \\ \sin(\pi\mu\tau)\sin(\pi(N-\mu)\tau), & \text{if m = n + 1, n - 1,} \\ & 1 \leq \text{ n } \leq \text{ N-1} \\ 0, & \text{otherwise} \end{cases}, \tag{3.10}$$

where $0 \leq \mu \leq N-1$ and $\tau = \frac{1}{N}$.

Santhanam and Vargas-Rubio focused their attention on the centered version of the DFT matrix operator $\mathbf{T}$ [14]. The eigenvalues of the commuter matrix $\mathbf{T}$ for the centered DFT are both real and unique and furnish the complete orthogonal set of DFT eigenvectors;

$$\mathbf{W}_{mn} = \frac{1}{\sqrt{N}} e^{(-\jmath \frac{2\pi}{N}(m-a)(n-a))}, \tag{3.11}$$

where the shift parameter $a = \frac{N-1}{2}$.

We plotted the eigenvectors and eigenvalues of the commuting matrix $\mathbf{T}$ to see whether the eigenvector and eigenvalues of the matrix look like those of the G-H operator. Figure 3.11(a) shows the 10^{th} eigenvector for $\mathbf{T}$-matrix for N = 256. From this, it is clear that an eigenvector of matrix $\mathbf{T}$ looks like a corresponding G-H function; however they are not exactly the same. The difference between these two is defined as the error-norm, and discussed next. Figure 3.11(b) shows the eigenvalues of $\mathbf{T}$-matrix. This plot says that the eigenvalues are not as linear as that of the G-H operator. Eigenvalues seems linear only for higher order.

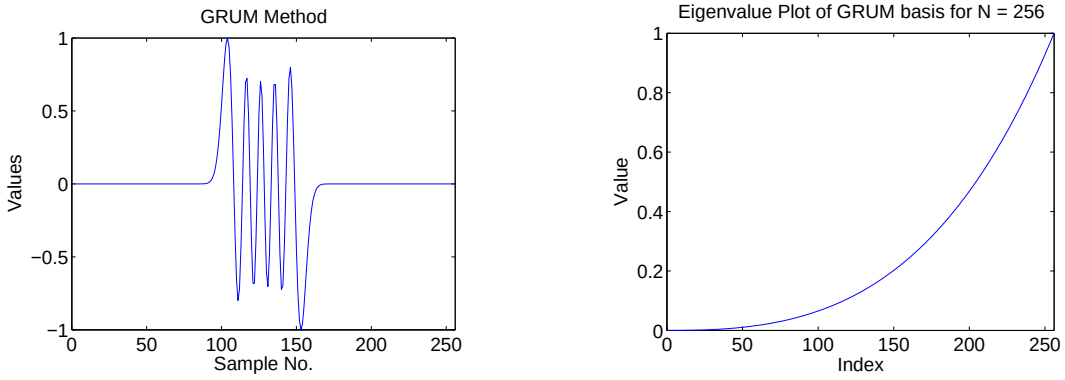

(a) (b)

Figure 3.11: (a)10^{th} eigenvector of the Grunbaum method for N=256 and (b) Eigenvalues of the Grunbaum method for N=256

We plotted the error-norm of the eigenvector of the matrix $\mathbf{T}$ for an order of 64 to check the error in representing the G-H function by the corresponding eigenvectors of matrix $\mathbf{T}$. Figure 3.12 shows the error-norm of the Grunbaum method for N = 64. From the plot, we can see that the error-norm for the Grunbaum method is slightly less in comparison to all the previously discussed methods. Therefore, we

can say that the eigenvectors of the **T**-matrix better resembles the corresponding G-H function than the eigenvectors of the three previously discussed methods.

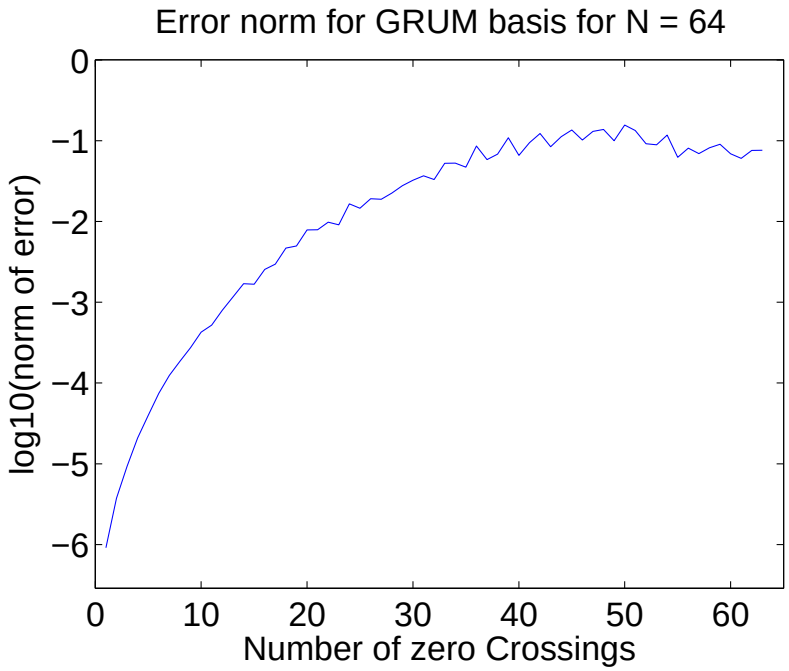

Figure 3.12: Error-norm for the Grunbaum method for N = 64

We also plotted the mapping region for the Grunbaum method to determine the region where there is a invertible mapping. Figure 3.13 shows the region in the $\alpha - \omega$ plane for the Grunbaum method where the mappings satisfied the connectivity and adjacency conditions for chirps of length N = 256, with a transform size $N \times N$, measured using $4N \times 4N$ chirps with center frequencies and chirp rates evenly spaced over the area shown in the figure. In the figure, black regions depict where the connectivity criteria is not satisfied whereas the grey region depict where the adjacency criteria is not satisfied. White regions indicate valid mapping regions for the Grunbaum method for N = 256.

As in the three previous cases, the invertible region for peak-to-parameter mapping is smaller in the case of the Grunbaum method. However, we can see some indication of a diamond-shape in this case, which we didn't see in the previous cases.

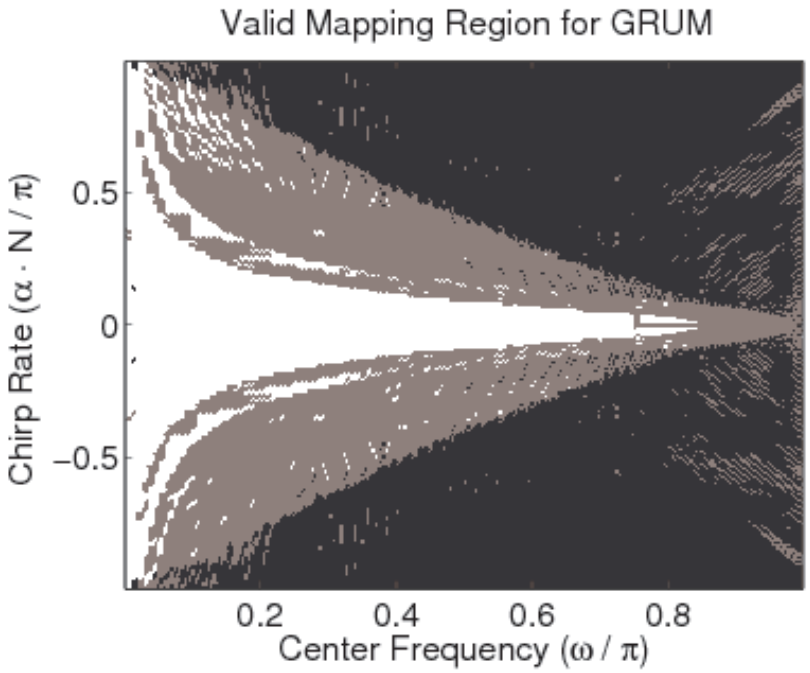

Figure 3.13: Valid mapping regions for the Grunbaum method for N = 256

3.5 The Quantum Mechanics in Finite Dimension (QMFD) Method

Santhanam et. al. defined a discrete version of the G-H differential operator **H** [31] that furnishes the basis for the centered version of the DFT matrix and simultaneously have eigenvalues and eigenvectors that very closely resemble those of the continuous G-H operator. They utilized concepts from quantum mechanics in finite dimensions [29] and [30], in the context of the discrete harmonic oscillator to the basis. The CDFT commuting matrix they defined is given as;

$$\mathbf{T} = c_1(\mathbf{P}^2 + \mathbf{Q}^2) + c_2\mathbf{C}_1^H\mathbf{C}_1 + c_3\mathbf{I}, \tag{3.12}$$

where $c_1 = 1, c_2 = -c_3 = -\frac{\pi^2}{N^2}$, N is the size of DFT matrix,

$\mathbf{P} = \mathbf{W}\mathbf{Q}\mathbf{W}^H$,

$\mathbf{Q}_{rr} = q[r] = \sqrt{\frac{2\pi}{N}}r,\ -\frac{N-1}{2} \leq r \leq \frac{N-1}{2}$,

$\{\mathbf{W}\}_{mn} = \frac{1}{\sqrt{N}}e^{(-\jmath\frac{2\pi}{N}(m-a)(n-a))}$ is a centered version of the DFT matrix ,

$a = \frac{N-1}{2},\ 0 \leq m, n \leq (N-1),$

$\mathbf{C}_1 = \mathbf{QP} - \mathbf{PQ}$ and

$\mathbf{I}$ is the identity matrix of dimension N.

We changed the range of r from $-\frac{N-1}{2} \leq r \leq \frac{N-1}{2}$ to the zero locations of the Nth order G-H function to see improvement in terms of linearity of the eigenvalues and the invertibility region in the peak-to-parameter mapping, and we found slight improvement in both the parameters. Therefore, we kept the values of r as the zero location of the N^{th} order G-H operator throughout the thesis, and we referred this method as *'modified QMFD'* or 'QMOD'.

We plotted the eigenvectors and eigenvalues of the commuter matrix $\mathbf{T}$ to see how close the eigenvectors were to the continuous G-H operator, and to see how linear the eigenvalues were. Figure 3.14(a) shows the 10^{th} eigenvector for matrix $\mathbf{T}$ for N = 256.

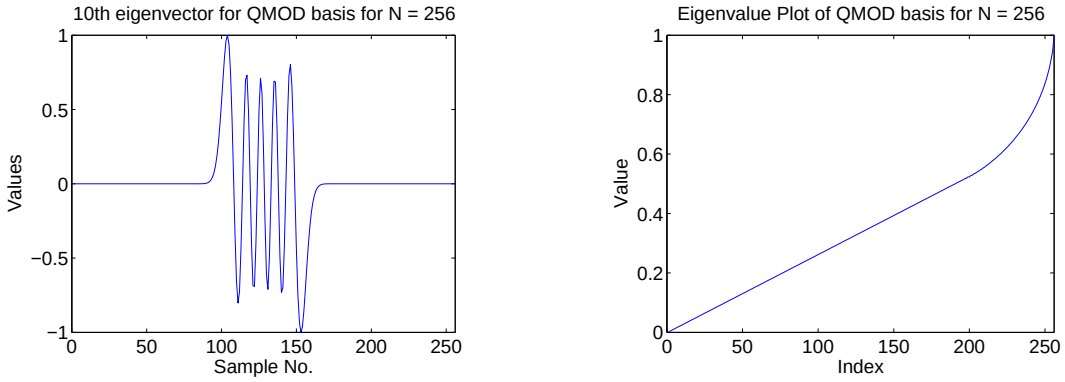

(a) (b)

Figure 3.14: (a)10^{th} eigenvector of the QMOD method for N=256 and (b) Eigenvalues of the QMOD method for N=256

From this, it is clear that an eigenvector of matrix $\mathbf{T}$ looks like a corresponding G-H function; however they are not exactly the same. Figure 3.14(b) shows the eigenvalues of matrix $\mathbf{T}$ for N = 256. This plot shows that the eigenvalues are almost linear except for the higher order index and it is clear that these eigenvalues for matrix $\mathbf{T}$ are closest to that of the continuous G-H operator in comparison to the eigenvalues of other previously discussed methods.

We plotted the error-norm of the eigenvectors of matrix $\mathbf{T}$ for an order of 64 to

check the error on representing the G-H function by the eigenvectors of matrix **T**. Figure 3.15 shows the error-norm for QMOD method for N = 64.

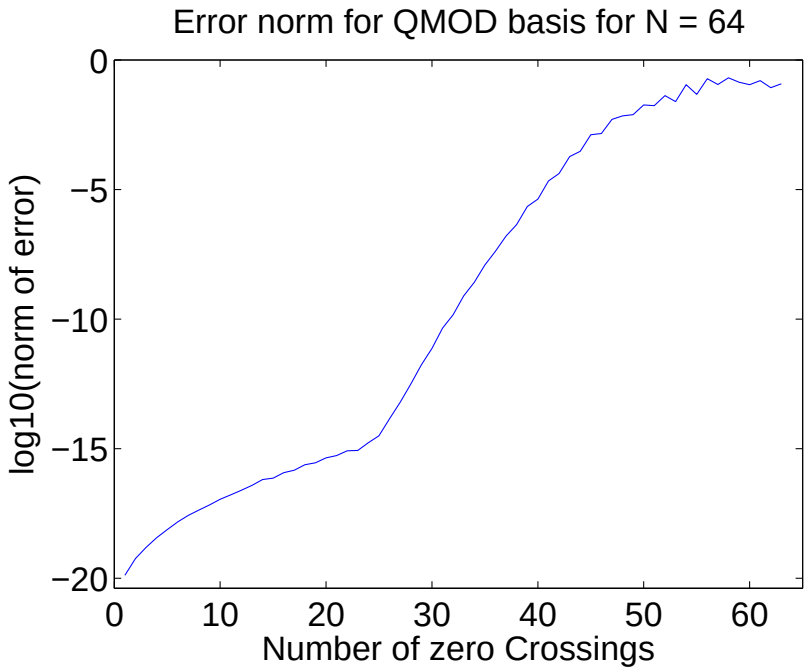

Figure 3.15: Error-norm for the QMOD method for N = 64

From this plot, we can see that the error-norm for the QMOD basis is very low for lower number of zero crossings in comparison to all the methods discussed above. Therefore, we can conclude that the eigenvectors of the QMOD method are the closest to the corresponding G-H function in comparison to the other four methods.

Figure 3.16 shows the region in the $\alpha - \omega$ plane for the QMOD method where the mappings satisfied the connectivity and adjacency conditions for chirps of length N = 256, with a transform size $N \times N$, measured using $4N \times 4N$ chirps with center frequencies and chirp rates evenly spaced over the area shown in the figure.

From this plot, it is clear that the invertibility region for the peak-to-parameter mapping, for the QMOD method is far better than that, for other previously discussed methods. The invertibility region for the QMFD method is almost the entire $\alpha - \omega$ plane. We can say that the mapping region for the QMOD is similar to the diamond shaped region shown in figure 3.4. Therefore, we can conclude that the QMOD method gives the best invertibility region for the peak-to-parameter mapping.

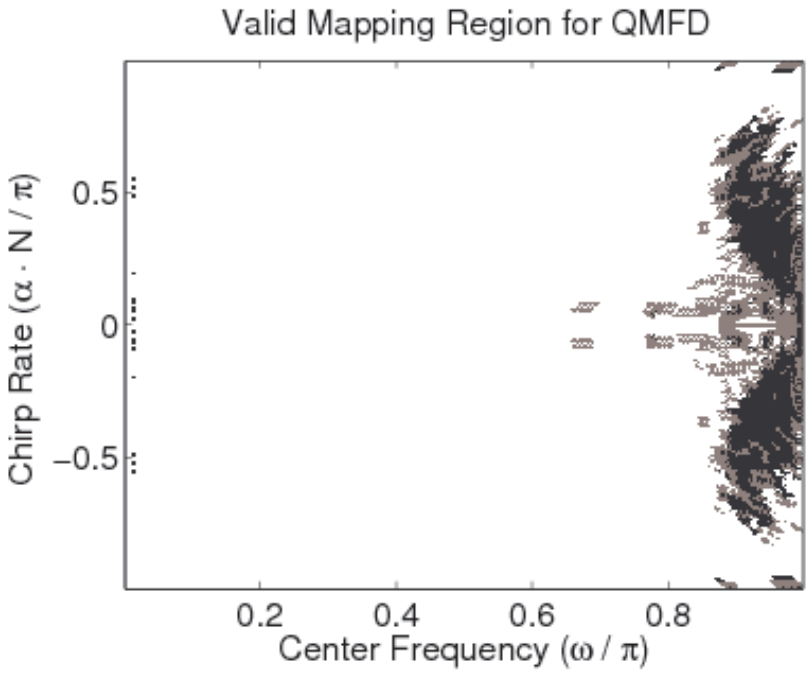

Figure 3.16: Valid mapping regions for the QMOD method for N = 256

3.6 The Joint Diagonalization Method

All the methods that we have been discussing so far are unable to produce eigenvalue spectrum that is strictly linear. Similarly, none of these approaches produces a valid mapping region for the entire $\alpha - \omega$ plane. We therefore combined the two approaches- the Grunbaum method and the QMOD method- to see whether this combination would produce more linearity in eigenvalues than that of either of the methods. Our intention in using joint diagonalization was also to get a better valid mapping region than that of the individual methods. This joint diagonalization is obtained using the matlab function 'eig'.

$$[V, D] = eig(TG, TQ), \tag{3.13}$$

where V = eigenvectors, D = digonalized eigenvalues, TG = CDFT matrix obtained using the Grunbaum method and TQ = CDFT matrix obtained using the QMOD method. The eigenvalues obtained from this joint diagonalization are depicted in figure 3.17. We then calculated the linearity of the eigenvalues obtained using the joint method, but we did not observe any improvement in linearity. In fact, the linearity decreased in comparison to the QMOD method.

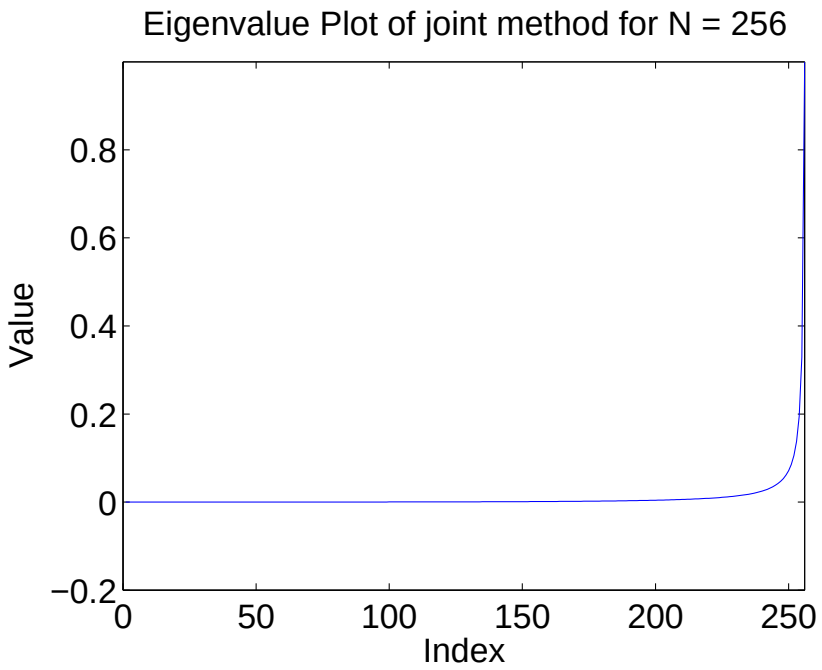

Figure 3.17: Eigenvalue plot for the joint diagonalization method

We also checked the valid mapping region corresponding to the joint method. Figure 3.18 shows the valid mapping region for the joint diagonalization method. Contrary to our expectation , we did not observe any improvement in the mapping region.

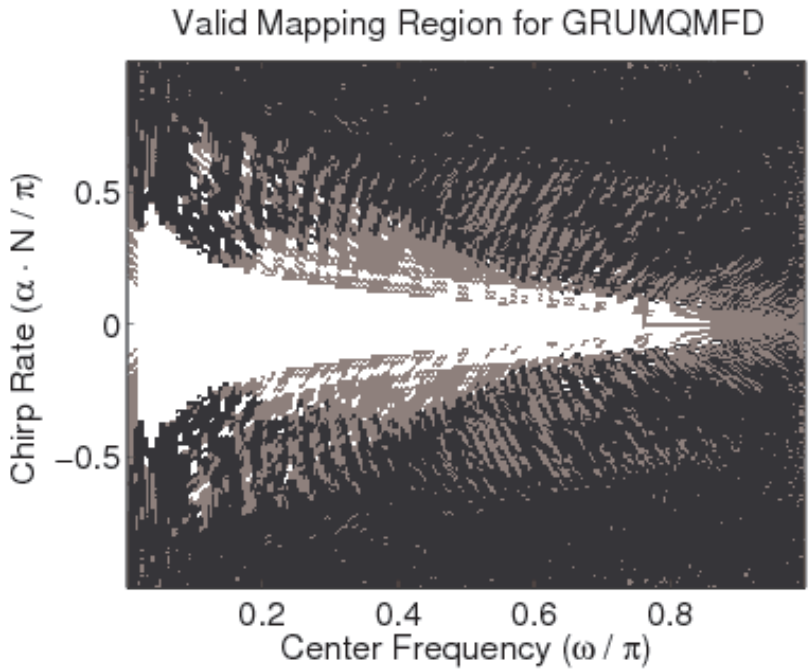

Figure 3.18: Valid mapping regions for the joint method for N = 256

From these observations, we can conclude that the joint diagonalization method would not produce any improvement in the linearity of eigenvalues and in the map-

ping region in comparison to the individual methods. In fact, the joint method produces the average results of the two methods, which are used in joint diagonalization.

3.7 Conclusion

In this chapter, we discussed the five different methods, which we used to generate a centered DFT matrix, whose eigenvectors and eigenvalues closely resemble those of the continuous G-H function. We also discussed some of the properties, such as eigenvalues, eigenvectors, error-norm, and invertibility regions for peak-to-parameter mapping, for each of those matrices.

Chapter 4

Comparison of Different CDFT Approaches

Pei, Hsue and Ding used the error-norm parameter to compare the eigenvectors of different DFT commuting matrices [13] to check the similarity between the eigenvector and the continuous G-H function. Serbes and Durak-Ata also used the same parameter for comparison in [12]. These analyses only determined how close the eigenvectors were to the sampled G-H function. As stated in [31], the linearity of the eigenvalues is another important parameter used to determine the closeness of the generating matrix to the G-H functions. Santhanam and Peacock introduced the valid mapping region criteria for peak-to-parameter mapping estimation [2]. In addition to the all the above mentioned parameters, we employed a few other parameters to find the best among the various CDFT commuting matrix approaches. In order to compare the different methods, we used the following parameters;

- Mainlobe-to-Sidelobe Ratio
- 10-dB Bandwidth
- Quality Factor
- Linearity of Eigenvalues
- Error-norm of the Eigenvectors
- Parameter Estimation Error
- Peak-to-Parameter Mapping Region

Using these seven parameters we tried to find the best CDFT commuting matrix among the five different methods to be used in chirp signal applications. As discussed in the previous chapter, the five methods used in this thesis are (1) the S-matrix method [11], (2) the Infinite order second derivative approximation method [13], (3) the bilinear transformation method [12], (4) the Quantum mechanics in finite dimension with modification (QMOD) [10] and (5) the Grunbaum method. As we have already discussed in the previous chapters, the eigenvectors of these commuting matrices are related to the continuous G-H function. Therefore, after this comparison we will be able to find the particular commuting matrix whose eigenvectors and eigenvalues are closest to those of the continuous G-H operator. In addition, this comparison tells us the quality of a peak which corresponds to the central frequency and chirp rate.

We considered a chirp signal to discuss the above mentioned parameters as;

$$x[n] = e^{\jmath(c_r m^2 + w_c n)},\ 0 \leq n \leq (N-1),\ m = n - \frac{N-1}{2}, \tag{4.1}$$

where, c_r = chirp rate and w_c = central frequency.

We assumed $c_r = 0.001$ and $w_c = 0$ for this analysis.

We used the MA-CDFRFT approach, as discussed in section 2.2.2, to see where the peak occurs for a given chirp rate and a central frequency. Then we took a row (where the peak occurs) of the MA-CDFRFT matrix to plot the peak that corresponds to the given chirp rate and the central frequency. Figure 4.1 describes the magnitude of the MA-CDFRFT of the above signal obtained from five different methods. From this plot, we can observe that we actually have two maxima because the CDFRFT at $\alpha + \pi$ is the reversed version of the CDFRFT at α.

We can observe from figure 4.1 that the least fringe occurs with the Grunbaum basis and the QMOD method, which means that the Grunbaum method results in the least side-lobes for MA-CDFRFT in comparison to the other four methods, whereas the bilinear transformation method, the higher order S-matrix method

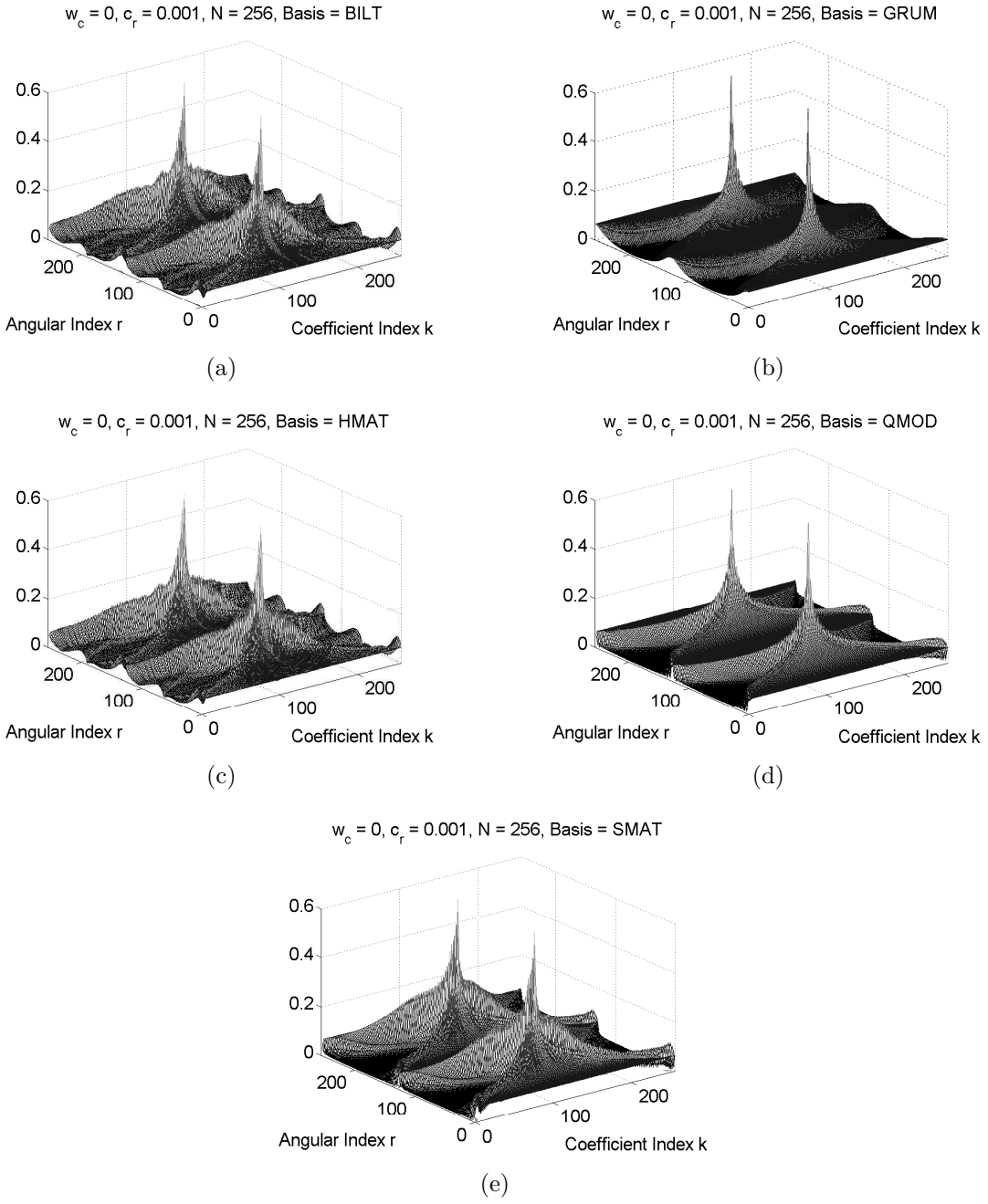

Figure 4.1: 3D plot of magnitude of MA-CDFRFT at $c_r = 0.001$ and $w_c = 0$ for N = 256 obtained from (a) Bilinear transformation method, (b) Grunbaum method, (c) Higher order S-matrix method, (d) QMOD method and (e) S-matrix method

and the D-S method produce larger sidelobes. We can see on a 2D plot of MA-CDFRFT that the two peaks on the magnitude plot of MA-CDFRFT occur at $r = 68$ and $r = 196$ for all the methods. We used only the lower half for our consideration. Then we took a slice of the MA-CDFRFT at $r = 68$. Figure 4.2 shows the slice of the MA-CDFRFT at $r = 68$ for all the methods.

From figure 4.2, it is clear that the sharpest peak is obtained with the QMOD

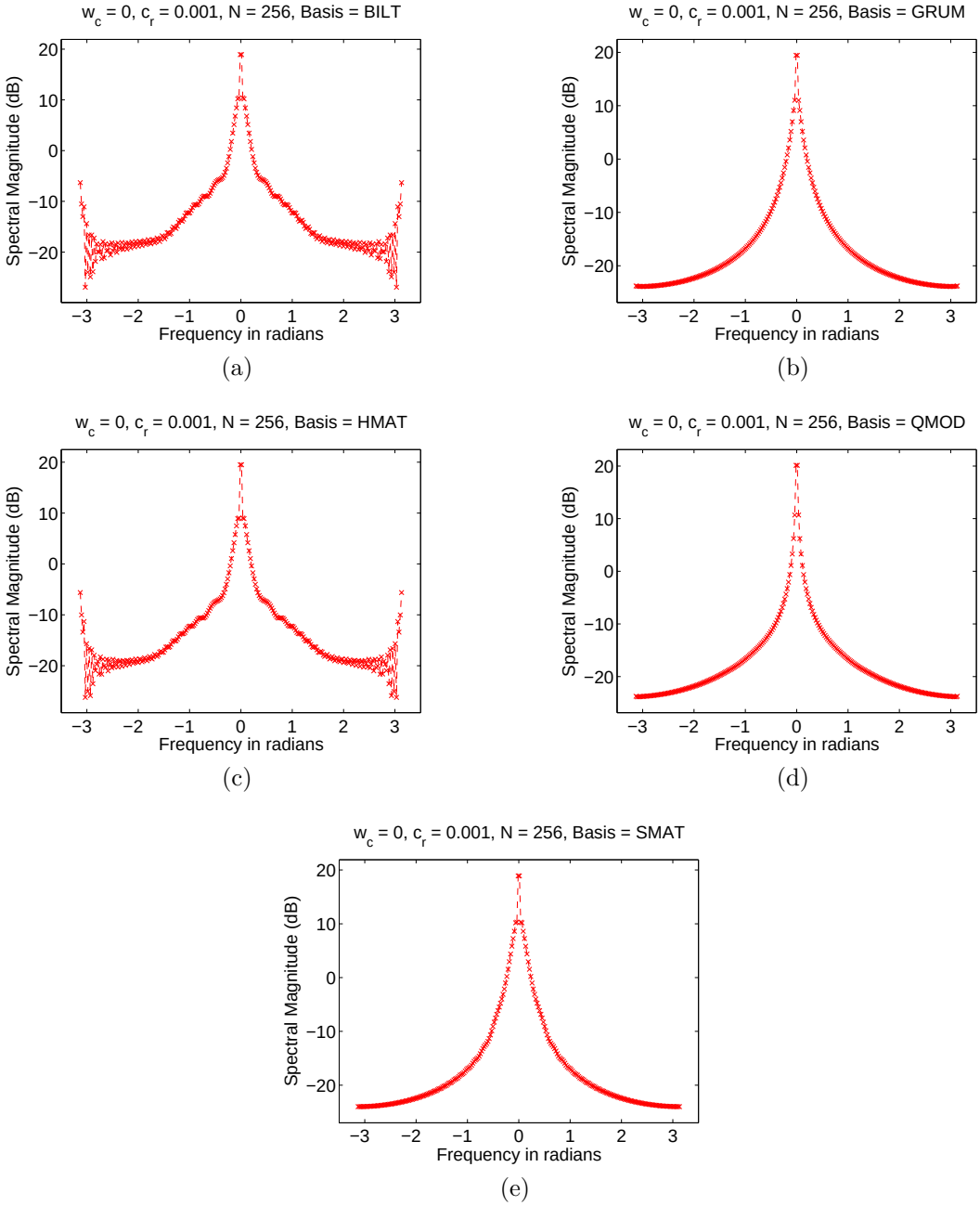

Figure 4.2: Plot of slice of MA-CDFRFT at r = 68 for $c_r = 0.001$, $w_c = 0$ and N = 256 obtained from (a) Bilinear transformation method, (b) Grunbaum method, (c) Higher order S-matrix method, (d) QMOD method and (e) S-matrix method

method. Note that the closer the is peak to the ideal delta function, the better the peak. Hence we can conclude that the QMOD method is the best among the five methods in terms of quality of the peak obtained from the MA-CDFRFT approach.

4.1 Mainlobe-to-Sidelobe Ratio

In antenna theory, main-lobe is the lobe containing the maximum power whereas side-lobes are the lobes that are not the main lobe, and the ratio of the power of these two lobes is defined as mainlobe-to-sidelobe ratio. For the purpose of this thesis, in the same fashion, the ratio of the peak value to the value of the second peak is defined as the mainlobe-to-sidelobe ratio. We can see those peak values and side-lobes in figure 4.2. In order to compute mainlobe-to-sidelobe ratio we first took the absolute value of the row of MA-CDFRFT matrix where peak occurs. We then found the highest peak as mainlobe and the second peak as sidelobe. Finally, we took the ratio of these two values as mainlobe-to sidelobe ratio. Figure 4.3 shows the mainlobe-to-sidelobe ratio for different combinations of c_r and w_c.

From these figures, it is clear that the mainlobe-to-sidelobe ratio (MLSLR) increases as N increases only in the case of the Grunbaum basis. Also, the QMOD method has a better mainlobe-to-sidelobe ratio in the case of zero central frequency until N = 512, whereas the Grunbaum method has a better mainlobe-to-sidelobe ratio in the case of non-zero central frequency. Therefore, we can conclude that the QMOD method and the Grunbaum method are the best choice among all the five methods towards attaininng a better mailobe-to-sidelobe ratio. We observed that the mainlobe-to-sidelobe ratio decreases for some methods for higher values of N. This is due to the fact that the MA-CDFRFT approach picks more side lobes as we increase transform size.

4.2 10-dB Bandwidth

In communication systems, the X-dB bandwidth of a communication channel is the part of the system's frequency response that lies within X-dB of the response at its peak, which in the pass-band filter case is typically at or near its center frequency, and in the lowpass filter is near 0 hertz. If the maximum gain is 0 dB, the X dB gain is the range where the gain is more than -X dB, or the attenuation

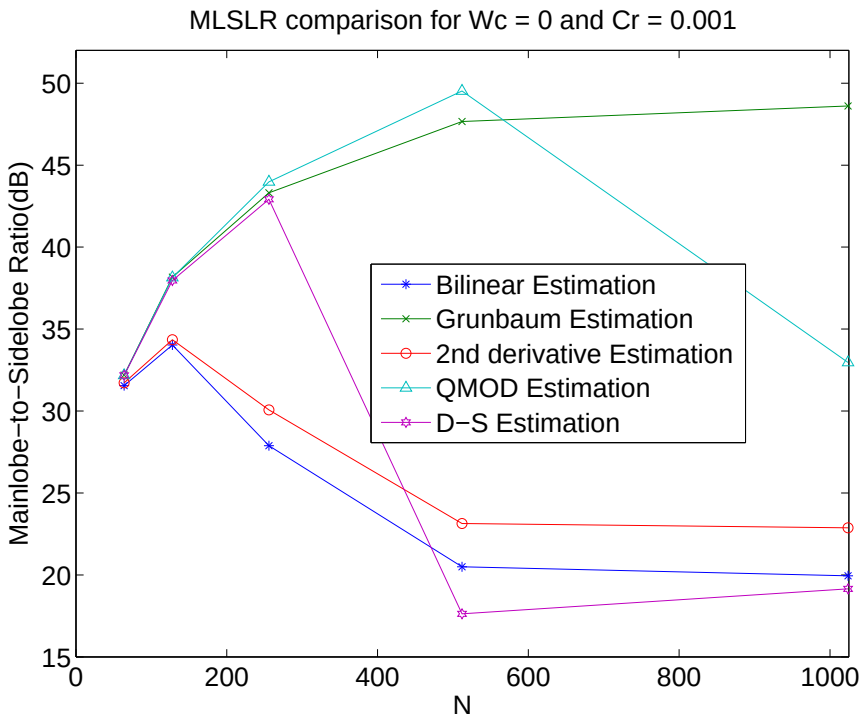

(a)

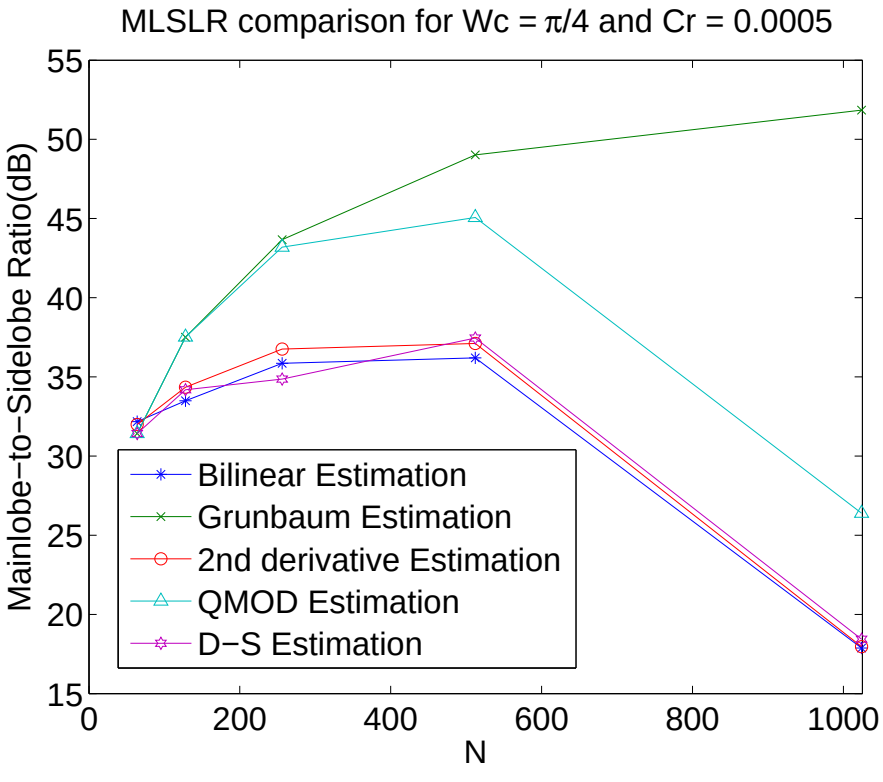

(b)

Figure 4.3: Mainlobe-to-Sidelobe ratio comparison for (a) $c_r = 0.001$ and $w_c = 0$ and (b) $c_r = 0.0005$ and $w_c = \frac{\pi}{4}$

is less than X dB. Similarly, 10-dB bandwidth, in this thesis, is defined as the

range of frequencies where the signal[1] has its value 10 dB below the peak value of the signal. Figure 4.4 shows the 10-dB bandwidth comparison for different combinations of c_r and w_c.

From these figures, we can see that the bandwidth continuously decreases only for the QMOD basis in the case of zero central frequency. And for non-zero central frequency, the bandwidth requirement continuously decreases as N increases. The bilinear transformation method and the S-matrix method have the least bandwidth requirements for non-zero central frequency.

4.3 Quality Factor

Quality factor, also known as Q-factor, is a dimensionless quantity which characterizes a signal's bandwidth relative to its central frequency. It measures the quality of the peak in relationship with central frequency. Mathematically, it is the ratio of the central frequency to the bandwidth of the signal. i.e.

$$Q - factor = \frac{w_c}{BW}, \tag{4.2}$$

where w_c = Central frequency and BW = Bandwidth of the signal.

We set the central frequency as $\frac{\pi}{4}$ and chirp rate as 0.0005 in equation (4.1) to find the Q-factor of the peaks for all the five methods. Therefore the signal used to find Q-factor became;

$$x[n] = e^{\jmath(0.0005m^2 + \frac{\pi}{4}n)}, \quad 0 \leq n \leq 255, \; m = n - \frac{255}{2}. \tag{4.3}$$

Figure 4.5 shows the quality factor comparison for $c_r = 0.0005$ and $w_c = \frac{\pi}{4}$. From this plot, it is clear that the Q-factor increases for all the bases as N increases,

[1]Signal refers to the magnitude of a slice of the MA-CDFRFT matrix at r = 36.

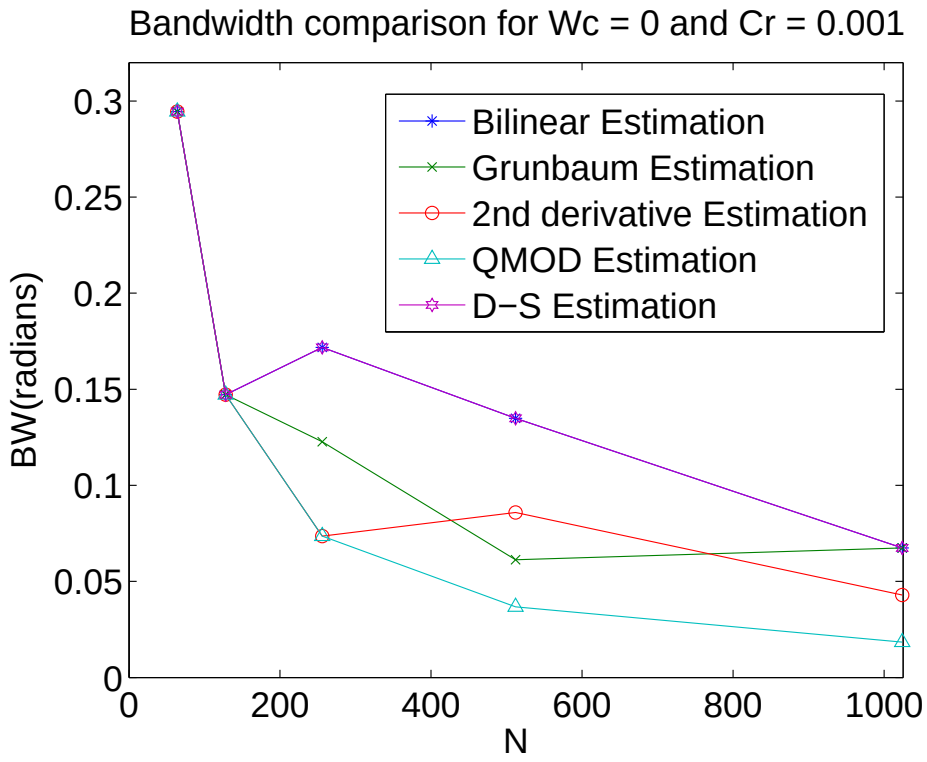

(a)

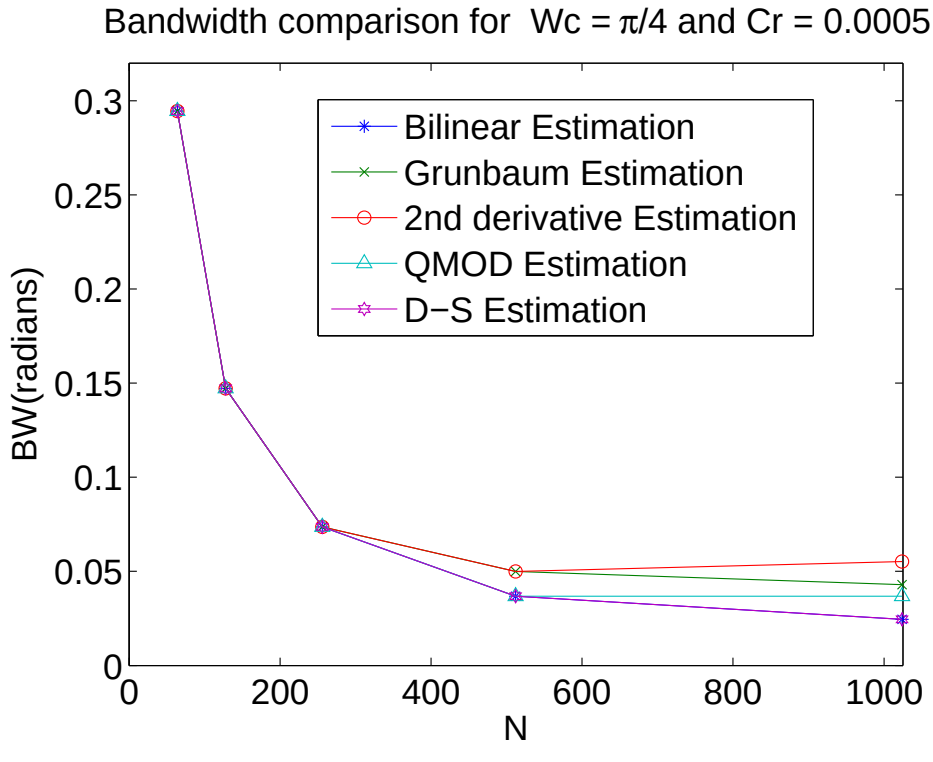

(b)

Figure 4.4: 10-dB Bandwidth comparison for (a) $c_r = 0.001$ and $w_c = 0$ and (b) $c_r = 0.0005$ and $w_c = \frac{\pi}{4}$

which is obvious from the previous section, because the lower bandwidth requirement for a fixed center frequency is equivalent to a higher quality factor. We

can see from the figure that the bilinear transformation method and the S-matrix method are the best choice for quality factor consideration.

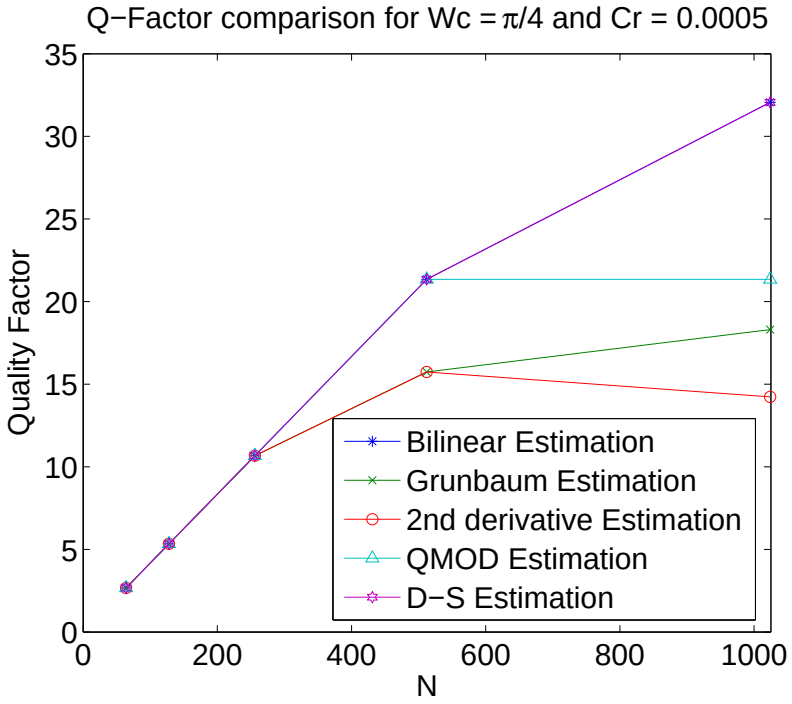

Figure 4.5: Quality factor comparison for $c_r = 0.0005$ and $w_c = \frac{\pi}{4}$

4.4 Linearity of Eigenvalues

Santhanam et. al. in [10] stated that eigenvalues of the G-H opertor is a linear function. Therefore the eigenvalues of the matrices obtained from all the five different approaches should be linear in nature in order to resemble the eigenvalues of the continuous G-H operator. As discussed in chapter-3, we first plotted the eigenvalues of the five different matrices to determine the extent of the linearity of eigenvalue spectrum. Then we calculated the percentage of number of points where the eigenvalues spread linearly for different values of N. Figure 4.6 shows the percentage of number of points where the eigenvalues are as linear as that of the continuous G-H operator.

From figure 4.6, it is evident that the eigenvalue spectrum from the QMOD method best resembles those of the continuous G-H operator. They are linear for about 80 percent of the total points which is far better than all other methods. The

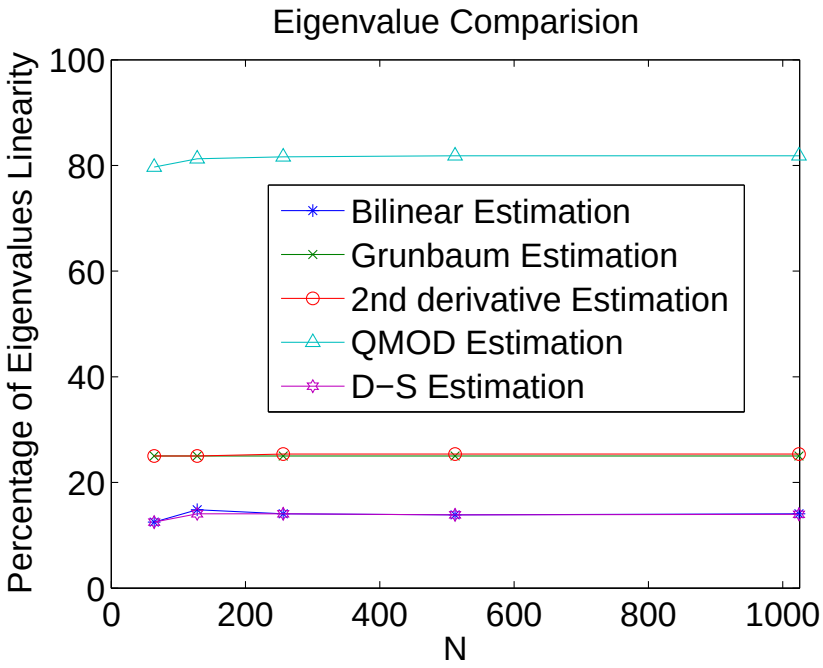

Figure 4.6: Percentage of number of points where eigenvalues are linear

linearity of the eigenvalue spectrum is directly related to the mapping region for peak-to-parameter mapping which we will discuss in a later section of this chapter.

4.5 Error-norm of the Eigenvectors

We have already observed in the previous chapter that the eigenvectors of the matrices that we discussed look like the corresponding G-H function; however they are not exactly the same. Pei, Hsue and Ding defined the error-norm of eigenvectors as the second norm of the difference between the eigenvectors obtained from the G-H like eigenvector[2] and the samples of its corresponding continuous G-H function [13]. We, therefore, plotted the error-norm of the eigenvectors for all the five different methods for N = 64 to determine eigenvectors of which matrix better resembled those of the continuous G-H operator. Figure 4.7 depicts the error-norm comparison for N = 64 for all the methods we discussed.

[2]G-H like eigenvectors are the eigenvectors of any of the matrices obtained from the five different approaches.

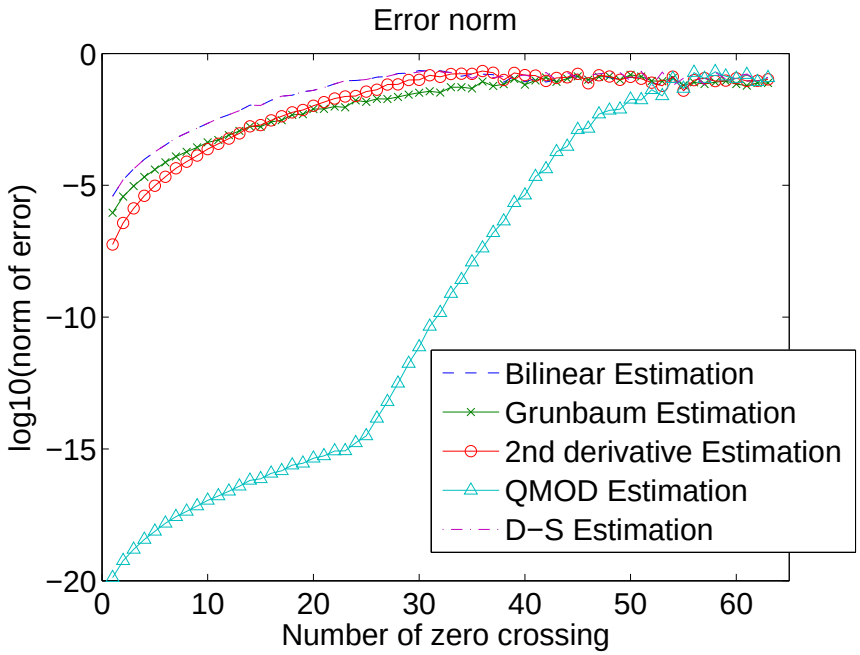

Figure 4.7: Error-norm comparison for N = 64

From this figure, it is clear that the error-norm increases as the number of zero crossings increases for all the methods, as we discussed in the previous chapter. We can also see that the QMOD method results in a very low error-norm in comparison to the other four methods. Therefore, eigenvectors of the QMOD matrix better resemble the eigenvectors of the corresponding G-H operator in comparison to the other four methods.

4.6 Parameter Estimation Error

Subspace decomposition techniques have been investigated for use in conjunction with the DFRFT with the aim of providing a robust and accurate estimation in the presence of noise [32]. Peacock and Santhanam discussed the chirp parameter estimation error using 2D peak picking [2]. We used parameter estimaion error as one of the bases for comparison of five proposed approaches. We measured the parameter estimation error of those five approaches and compared them to the Cramer-Rao lower bound and resolution bound. Figure 4.8 shows the parameter estimation error using 2D peak picking for central frequency and chirp rate, for N = 256.

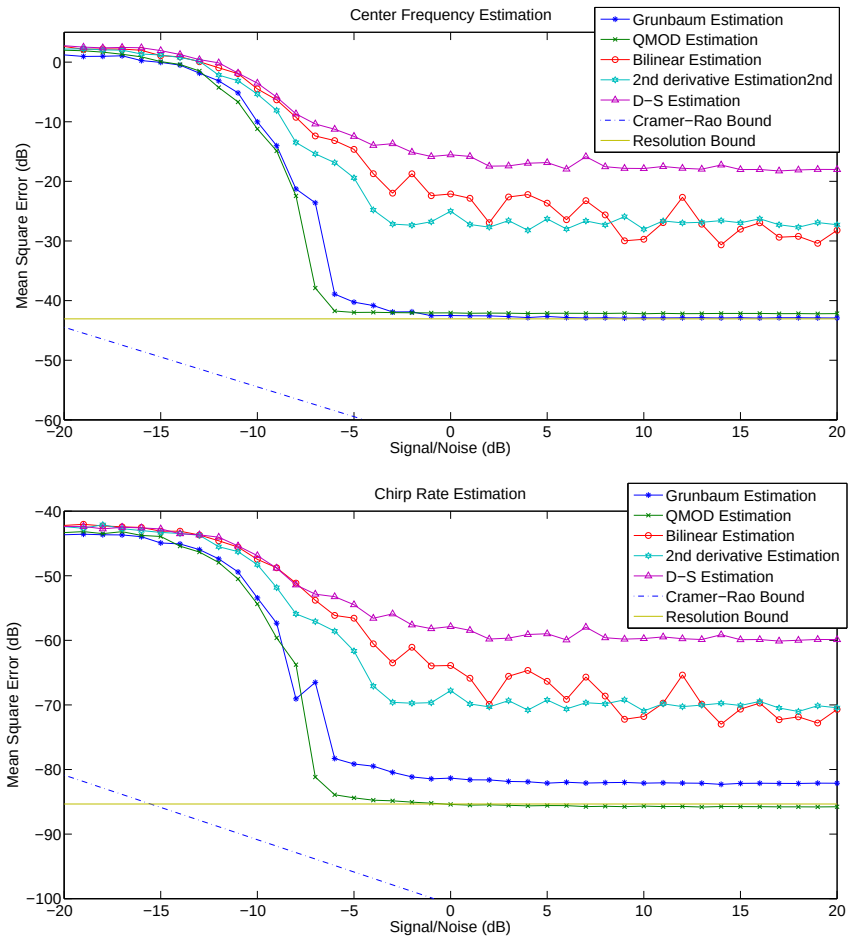

Figure 4.8: 2D parameter estimation error: The MSE was calculated at each SNR using 1000 chirps of length N = 256, in the 'safe' range of $|\alpha|(N-1)+|w| = IF < 0.85\pi$.

From this figure, we can see that the detection error for the QMOD method attains the resolution bound for higher SNR for both center frequency estimation and chirp rate estimation, and the error for the Grunbaum method is close to that of the QMOD method. However the other three methods result in significantly more parameter estimation errors. This is because the peak-to-parameter mapping depicts multiple disconnected regions of chirp parameters mapping to the same peak location. We can also see that, both the center frequency estimation and chirp rate estimation for the bilinear transformation method do not decrease as gradually as in other methods. This is because of the fact that the particular combination of center frequency and chirp rate, where the mean square error goes up, does not lie withn the invertible mapping region. Figure 4.9 shows the parameter estimation error calculated using the cross-hair technique combined with the minimum-norm-subspace technique. From this figure, we can see that the chirp parameter estimaion error for the QMOD method approaches the Cramer-

Rao lower bound for chirp parameter estimation [26]. From this analysis, we can conclude that either of these techniques has more success using the QMOD basis.

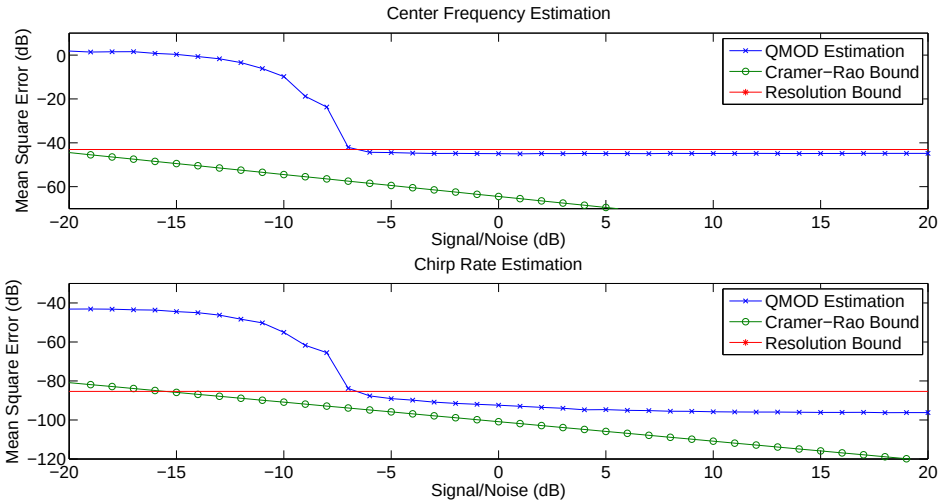

Figure 4.9: Cross-hairs estimation error: The MSE was calculated at each SNR using 1000 chirps of length N = 256, in the 'safe' range of $|\alpha|(N-1)+|w| = IF < 0.85\pi$. A transform of size NXN was used, refined using minimum norm subspace decomposition and FFT of size R = 4096.

4.7 Peak-to-Parameter Mapping Region

As we already discussed in section 3.1, application of the DFRFT to chirp parameter estimation is not meaningful if a complete analysis of the invertibility of mapping is ignored. Therefore we looked at the peak-to-parameter mapping region in the $\alpha-\omega$ plane to see where the mappings satisfied the connectivity and adjacency conditions. The connectivity criteria is satisfied when the set of all chirp parameters that map to a single location in the chirp-rate versus center-frequency plane form a connected set, and adjacency criteria is satisfied when locations which are adjacent in the transform plane map to adjacent regions in the chirp parameter space. In the previous chapter, we calculated the mapping regions where both connecticity and adjacency criteria were satisfied for all the five methods. We calculated the percentage of pixels in which both the connectivity and adjacency conditions were satisfied. Upon doing this, we had a clear idea of which method, among the five proposed methods, had the best valid mapping region in comparison to the expected mapping region shown in figure 3.4. Figure 4.10 depicts the percentage of pixels in $\alpha-\omega$ plane in which both connectivity

and adjacency criteria are fulfilled.

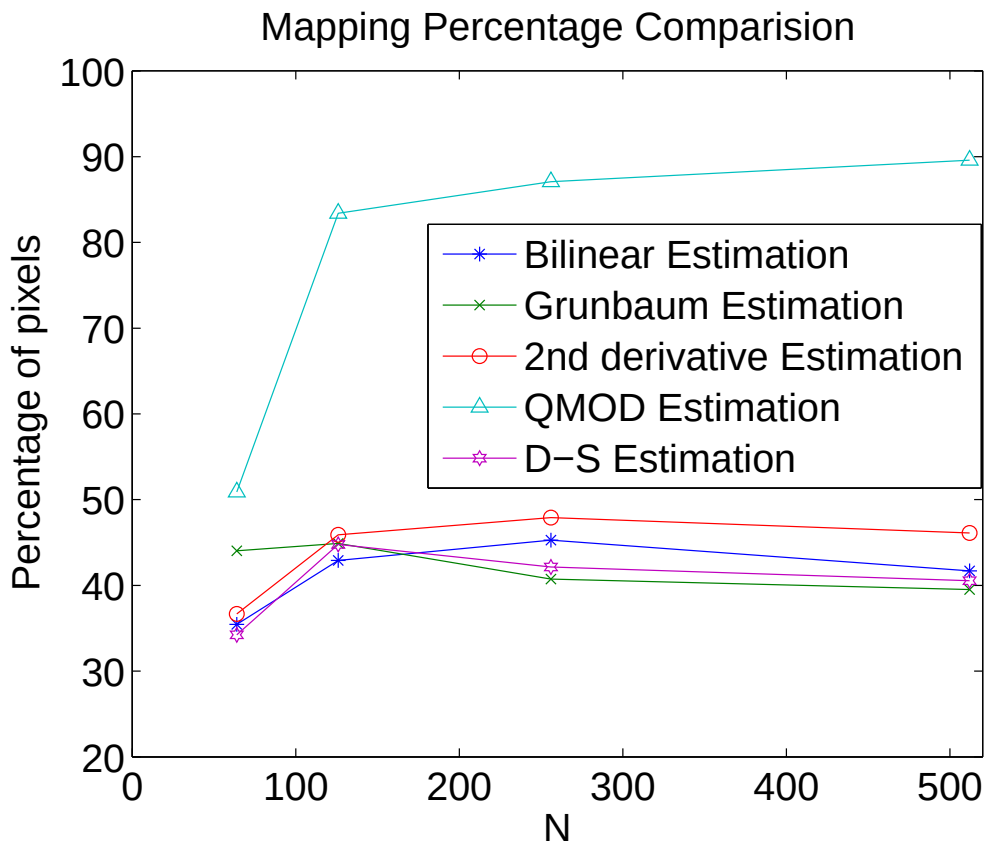

Figure 4.10: Plot of percentage of pixels in $\alpha - \omega$ plane where both connectivity and adjacency criteria are fulfilled

From these mapping regions, we can see that the connectivity and adjacency conditions are not fulfilled for large regions in the case of the bilinear transformation method, the S-matrix method and the higher order S-matrix method. The regions in which these two conditions are violated overlap in these three cases. In the case of Grunbaum method, we can see that, the two conditions are not satisfied in two different regions. The connectivity criteria is almost satisfied in the diamond region for the Grunbaum method, but the adjacency criteria is not satisfied as expected in the diamond region. Finally, both the criteria are satisfied in almost entire region of the $\alpha - \omega$ plane for the case of the QMOD method.

From this comparison, we can also see that the QMOD is the only method in which the percentage of pixels satisfying both the connectivity and adjacency criteria, increases as N increases. This fact is further related to the linearity of the eigenvalue spectrum. We saw in section 4.4 that the linearity of the eigenvalue spectrum increases when N increases only in the case of the QMOD basis. We

also observed that the percentage of eigenvalue linearity for the QMOD method is far above than that of all other methods. From figure 4.10, we can see that the percentage of pixels reaches almost 90% for the QMOD method for N = 512, which is far better than all the other methods. This confirms the fact that the QMOD basis produces the least estimation error because it has the largest valid peak-to-parameter mapping region in the $\alpha - \omega$ plane. We can also say that the valid mapping region will cover the entire $\alpha - \omega$ plane if N is sufficiently large for the QMOD basis. Note that if the valid mapping region spreads over the entire $\alpha - \omega$ plane, it will correspond to the case in which there is no estimation error for both center frequency and chirp rate. This condition of no estimation error is equivalent to the expected mapping region shown in figure 3.4.

4.8 Conclusion

In this chapter, we discussed different performance metrics to find the best method for chirp signal applications. From these comparisons, we found that the QMOD method produces the best results for all the parameters we discussed. Therefore, we can conclude that the QMOD method is the most appropriate method to use in chirp signal applications among all the five methods.

Chapter 5

Conclusions and Future Works

5.1 Conclusions

In this thesis, we studied the centered DFRFT, its properties, the nature of its eigenvalues and eigenvectors, and its relationship with linear chirp signals. The main objective of this thesis was to find the best algorithm to use for the computation of the centered version of DFRFT. We studied some properties of each of the CDFRFT matrices that were obtained from different approaches. We looked at the eigenvalues and eigenvectors of those matrices to see whether or not they resembled those of the continuous G-H operator. We also calculated the error-norm of eigenvectors to determine whether or not there were any deviations of those eigenvectors from those of the corresponding G-H operator. In addition, we calculated the chirp parameter estimation errors using 2D peak detection in the MA-CDFRFT chirp-rate versus central-frequency plane. Finally, we measured the peak-to-parameter mapping region where connectivity and adjacency criteria were satisfied.

The main findings of this thesis can be summarized as;

- Among all the five methods discussed in this thesis, the QMOD method, a method in which the diagonal matrix $\mathbf{Q}$ takes its diagonal as the zero crossings

of the Nth order G-H function instead of taking its diagonal as equally spaced values in between $-\frac{N-1}{2}$ and $\frac{N-1}{2}$ used in the conventional QMFD method, produces the sharpest peak for single chirp application. This result was verified by using different metrics such as mainlobe-to-sidelobe ratio, 10-dB bandwidth, and quality factor.

- The QMOD method produces the best linearity on eigenvalues, which confirms the fact that the eigenvalues obtained from the QMOD method are closest to the eigenvalues of the continuous G-H operator.

- The QMOD method results in less error-norm than the other methods, which confirms that the eigenvectors of the QMOD matrix are closest to that of the continuous G-H operator.

- As is evident from the previous chapter, the QMOD method produces the least parameter estimation error for both center frequency estimation and chirp rate estimation. This estimation error almost attains the Camer-Rao lower bound when it is calculated for the QMOD method in combination with the cross-hair estimation technique.

- As we saw in the previous chapter, the QMOD method has an invertibility region of almost 90% of the $\alpha - \omega$ plane, which is far better than those of the other four methods.

- Deviation from a fully linear eigenvalue spectrum produces a large proportion of peak-to-parameter mapping where the invertibility criteria are violated.

- Loss of invertibility results in larger chirp parameter estimation error.

5.2 Future Work

We have seen that none of the approaches we discussed is able to produce the entire region of the $\alpha - \omega$ plane for peak-to-parameter mapping. This creates error in chirp parameter estimation. We think that the future extension of this

thesis could be focused on how to completely avoid parameter estimation error. The approach that, we believe, could be used is described a s follows:

- Find a CDFT commuting matrix which has a completely linear eigenvalue spectrum. This spectrum is same as those of the eigenvalue spectrum of the corresponding G-H operator. However, it is practically impossible to obtain a CDFT commuting matrix whose eigenvalue spectrum is completely linear.
- Once we have such a matrix, we will be able to produce an invertibility region of entire the $\alpha - \omega$ plane for peak-to-parameter mapping. This provides us with an easier way to do peak-to-parameter mapping by using a relationship between chirp parameters (w_c and c_r) and peak location(r).
- Once there is an entire $\alpha - \omega$ plane of invertibility region, there will be no parameter estimation error for two reasons. The first reason is that the set of all chirp parameters that map to a single location in the chirp-rate versus center-frequency plane forms a connected set. This will satisfy the connectivity criteria for the peak-to-parameter mapping. The second reason is that the locations which are adjacent in the transform plane map to adjacent regions in the chirp parameter space.

There are also some other research dimensions that could be considered as extensions of this thesis work, which are applications of DFRFT.

Chirp signals are sinusoidal waveforms with linearly changing instantaneous frequency. They find wide applications in radar systems, including synthetic aperture radar. A robust method of multicomponent parameter estimation would enable the estimation of the vibrational frequency of a target and improve estimation performance in the presence of clutter. The DFRFT shows promise in multicomponent chirp parameter estimation, as it generates a strong peak for each chirp whose location in the 2D transform plane corresponds to the specific center frequency and chirp rate.

A discrete version of the fractional sine and cosine transforms has been proposed in [37], and it is therefore expected that significant progress will be made in the

area of image processing. Some interesting applications of FRFT in the areas of control systems and telecommunications are now being probed. It is, therefore, quite reasonable to expect that the FRFT will eventually replace the Fourier transform as the single most effective tool in signal analysis. Thus it becomes exceedingly important both to develop and to implement the discrete version of the FRFT.

Bibliography

[1] V. Namias, The Fractional Order Fourier Transform And Its Application To Quantum Mechanics, *Journal of the Institute of Mathematics and its Applications*, Vol. 25, Pages 241 - 265, (April 1980)

[2] D.J. Peacock and B. Santhanam, Comparison Of Centered Discrete Fractional Fourier Transform For Chirp Parameter Estimation, *Proc. of IEEE DSP/SPED Workshop*, (August 2013).

[3] B. Santhanam and J.H. McClellan, The Discrete Rotational Fourier Transform, *IEEE Transactions In Signal Processing*, Vol. 44, No. 4, (April 1996).

[4] J.H. McClellan and T.W. Parks, Eigenvalues And Eigenvectors Of The Discrete Fourier Transformation, *IEEE Transactions on Audio and Electromagnetics*, Vol. 20, No. 1, (March 1972)

[5] G. Strang, Linear Algebra And Its Application, *Academic Press*, New York, (1995)

[6] S. Pei and M. Yeh, Improved Discrete Fractional Fourier Transform, *Optics Letters*, Vol. 22, No. 14, (July 1997)

[7] J.G. Vargas-Rubio and B. Santhanam, On The Multiangle Centered Discrete Fractional Fourier Transform, *IEEE Signal Processing Letters*, Vol. 12, No. 4, (April 2005)

[8] D. H. Mugler and S. Clary, Discrete Hermite Functions And The Fractional Fourier Transform, *In International Conference on Sampling Theory and Application*, Pages 303 - 308, (2001)

[9] M.L. Mehta, Eigenvalues And Eigenvectors Of The Finite Fourier Transform, *Journal of Mathematical Physics* 28, 781, (1987)

[10] B. Santhanam and T.S. Santhanam, Discrete Gauss Hermite Functions And Eigenvectors Of The Centered Discrete Fourier Transform, *Proc. of ICASSP 2007, Honolulu*, Pages 418 - 422, (April 2007)

[11] B.W. Dickinson and K. Steiglitz, Eigenvectors And Functions Of The Discrete Fourier Transform, *IEEE Transactions on Acoustics, Speech and Signal Processing*, Vol. 30, No. 1, (February 1982)

[12] A. Serbes and L. Dural-Ata, Eigenvectors Of The Discrete Fourier Transform Based On The Bilinear Transform, *Eurasia Journal on Advances in Signal Processing*, Vol. 2010 Article ID. 191085

[13] S.C. Pei, W.L. Hsue and J.J. Ding, DFT-Commuting Matrix With Arbitrary Or Infinite Order Second Derivative Approximation, *IEEE Transactions on Signal Processing*, Vol. 51, No. 1, (January 2009)

[14] B. Santhanam and J.G. Vargas-Rubio, On the Grunbaum Commuter Based Discrete Fractional Fourier Transform, *Proc. of ICASSP-04, Montreal, Canada*, Vol. II, Pages 641 - 644, (May 2004)

[15] J.G. Vargas-Rubio and B. Santhanam, The Centered Discrete Fractional Fourier Transform And Linear Chirp Signals, *Proc. of 11th IEEE DSP & DSP Education Workshop, Taos Ski Valley, New Mexico*, Pages 163 - 167, (August 2004)

[16] C. Candan, M.A. Kutay and H.M. Ozatkas, The Discrete Fractional Fourier Transform, *IEEE Transactions On Signal Processing*, Vol. 48, No. 5, Pages 1329 - 1337, (May 2000)

[17] G. Cariolaro, T. Erseghe, P. Kraniauskas, and N. Laurenti, A United Framework For The Fractional Fourier Transform, *IEEE Transactions on Signal Processing*, Vol. 46, No. 12, Pages 3206 - 3219, (December 1998)

[18] G. Cariolaro, T. Erseghe, P. Kraniauskas and N Laurenti, Multiplicity Of Fractional Fourier Transforms And Their Relationships, *IEEE Transactions on Signal Processing*, Vol. 48, No. 1, Pages 227 - 241, (January 2000)

[19] L. B. Almeida, An Introduction To The Angular Fourier Transform, *In Proceedings of International Conference on Acoustics, Speech and Signal Processing*, Vol. 3, Pages 257 - 260, (April 1993)

[20] H.M. Ozaktas, Z. Zalevski, and M.A. Kutay, The Fractional Fourier Transform With Applications In Optics And Signal Processing, *New York: Wiley and Sons*, (2001)

[21] L. Durak and O. Arkan, Short-Time Fourier Transform: Two Fundamental Properties And An Optimal Implementation, *IEEE Transaction on Signal Processing*, Vol. 51, No. 5, Pages 1231 - 1242, (2003)

[22] A. Serbes and L. Durak, Optimum Signal And Image Recovery By The Method Of Alternating Projections In Fractional Fourier Domains, *Communications in Nonlinear Science and Numerical Computer*, (2009)

[23] C.D. Luigi and E. Moreau, An Iterative Algorithm For Estimation Of Linear Frequency Modulate Signal Parameters, *IEEE Signal Process. Letters*, Vol. 9, Pages 127 - 129, (2002)

[24] M.T. Hanna, N.P.A. Seif and W.A.E.M. Ahmed, Hermite-Gaussian-Like Eigenvectors Of The Discrete Fourier Transform Matrix Based On The Singular-Value Decomposition Of Its Orthogonal Projection Matrices, *IEEE*

Trans. Circ. System- I: Regular Papers, Vol. 51, No. 11, Pages 2245 - 2254, (2004)

[25] S.C. Pei, M.H. Yeh and C.C. Tseng, Discrete Fractional Fourier Transform Based On Orthogonal Projections, *IEEE Trans. Signal Processing*, Vol. 47, No. 5, Pages 1335 - 1348, (1999)

[26] D.J. Peacock and B. Santhanam, Multicomponent Subspace Chirp Parameter Estimation Using Discrete Fractional Fourier Analysis, *Processing of IASTED Conference on SIP-2011*, Pages 326 - 333, (December 2011)

[27] F.A. Grunbaum, The Eigenvectors Of The Discrete Fourier Transform: A Version Of The Hermite Functions, *Journal of Mathematical Analysis and Applications*, Vol. 88, Pages 355 - 363, (1982)

[28] S. Clary and D.H. Mugler, Shifted Fourier Matrices And Their Tri-Diagonal Commutors, *SIAM Journal Matrix Analysis & Applications*, Vol. 24, No. 3, Pages 809 - 821, (2003)

[29] R. Jagannathan, T.S. Santhanam, and R. Vasudevan, Finite Dimensional Quantum Mechanics Of A Particle, *International Journal of Theoretical Physics*, Vol. 20, Pages 755 - 783, (1981)

[30] T.S. Santhanam and A.R Tekumalla, Quantum Mechanics In Finite Dimensions, *Foundation of Physics*, Vol. 6, No. 5, Pages 583 - 587, (1976)

[31] B. Santhanam and T.S. Santhanam, On discrete Gauss-Hermite Functions And Eigenvectors Of The Discrete Fourier Transform, *Signal Processing, Elsevier Science*, Vol. 88, No. 6, Pages 2738 - 2746, (November 2008)

[32] B. Santhanam and M. Hayat, On A Pseudo-Subspace Framework For Discrete Fractional Fourier Transform Based Chirp Parameter Estimation, *Processing of IEEE DSP/SPE Workshops*, Pages 360 - 363, (2011)

[33] C. Candan, On Higher Order Approximations For Hermite?aussian Functions And Discrete Fractional Fourier Transforms, *IEEE Signal Processing Letters*, Vol. 14, No. 10, (October 2007)

[34] H.M. Ozaktas, O. Arikan, M.A. Kutay and G. Bozdagi, Digital Computation Of The Fractional Fourier Transformation, *IEEE Trans. Signal Processing*, Vol. 44, No. 9, Pages 2141 - 2150, (September 1996)

[35] X.G. Xia, Discrete Chirp Fourier Transform And Its Application To Chirp Estimation, *IEEE Trans. Signal Processing*, Vol. 48, No. 11, Pages 3122 - 3133, (November 2000)

[36] H.M.Ozaktas, B.Barshan, D.Mendlovic, and L.Onural, Convolution, Filtering, And Multiplexing In Fractional Fourier Domains And Their Relation To Chirp And Wavelet Transform, *J. Opt. Soc. Amer*, Vol. 11, Pages 547 - 559, (1994)

[37] S.C. Pei, M.H. Yeh, The Discrete Fractional Cosine And Sine Transforms, *IEEE Transactions of Signal Processing*, Vol. 49, No.6, Pages 1198 - 1207, (2001)